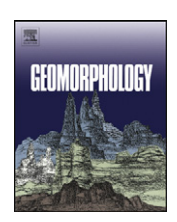


Contents lists available at ScienceDirect

Geomorphology

journal homepage: www.elsevier.com/locate/geomorph



The size, distribution, and mobility of landslides caused by the 2015 M_w7.8 Gorkha earthquake, Nepal☆



Kevin Roback ^a, Marin K. Clark ^{a,*}, A. Joshua West ^b, Dimitrios Zekkos ^c, Gen Li ^b, Sean F. Gallen ^d, Deepak Chamlagain ^e, Jonathan W. Godt ^f

- ^a Department of Earth and Environmental Sciences, University of Michigan, Ann Arbor, MI 48109, USA
- ^b Department of Earth Sciences, University of Southern California, Los Angeles, CA 90089, USA
- ^c Department of Civil and Environmental Engineering, University of Michigan, Ann Arbor, MI 48109, USA
- ^d Department of Earth Sciences, ETH Zurich, Sonneggstrasse 5, 8092 Zurich, Switzerland
- ^e Department of Geology, Tri-Chandra Multiple Campus, Tribhuvan University, Kathmandu, Nepal
- f Natural Hazards Mission Area, Landslide Hazards Program, U.S. Geological Survey, Denver, CO 80225, USA

ARTICLE INFO

Article history: Received 12 August 2016 Received in revised form 16 January 2017 Accepted 22 January 2017 Available online 16 February 2017

ABSTRACT

Coseismic landslides pose immediate and prolonged hazards to mountainous communities, and provide a rare opportunity to study the effect of large earthquakes on erosion and sediment budgets. By mapping landslides using high-resolution satellite imagery, we find that the 25 April 2015 M_w7.8 Gorkha earthquake and aftershock sequence produced at least 25,000 landslides throughout the steep Himalayan Mountains in central Nepal. Despite early reports claiming lower than expected landslide activity, our results show that the total number, area, and volume of landslides associated with the Gorkha event are consistent with expectations, when compared to prior landslide-triggering earthquakes around the world. The extent of landsliding mimics the extent of fault rupture along the east-west trace of the Main Himalayan Thrust and increases eastward following the progression of rupture. In this event, maximum modeled Peak Ground Acceleration (PGA) and the steepest topographic slopes of the High Himalaya are not spatially coincident, so it is not surprising that landslide density correlates neither with PGA nor steepest slopes on their own. Instead, we find that the highest landslide density is located at the confluence of steep slopes, high mean annual precipitation, and proximity to the deepest part of the fault rupture from which 0.5-2 Hz seismic energy originated. We suggest that landslide density was determined by a combination of earthquake source characteristics, slope distributions, and the influence of precipitation on rock strength via weathering and changes in vegetation cover. Determining the relative contribution of each factor will require further modeling and better constrained seismic parameters, both of which are likely to be developed in the coming few years as post-event studies evolve. Landslide mobility, in terms of the ratio of runout distance to fall height, is comparable to small volume landslides in other settings, and landslide volume-runout scaling is consistent with compilations of data on larger slope failures. In general, the size ratios of landslide source area to full landslide area are smaller than global averages, and hillslope length seems to largely control runout distance, which we propose reflects a topographic control on landslide mobility in this setting. We find that landslide size dictates runout distance and that more than half of the landslide debris was deposited in direct connection with stream channels. Connectivity, which is defined as the spatial proximity of landslides to fluvial channels, is greatest for larger landslides in the high-relief part of the High Himalaya. Although these failures are less abundant than those at lower elevations, they may have a disproportionate impact on sediment dynamics and cascading hazards, such as landslide reactivation by monsoon rainfall and landslide dams that lead to outburst floods. The overall high fluvial connectivity of coseismic landsliding in the Gorkha event suggests coupling between the earthquake cycle and sediment/geochemical budgets of fluvial systems in the Himalaya.

© 2017 The Authors, Published by Elsevier B.V. This is an open access article under the CC BY-NC-ND license (http://creativecommons.org/licenses/by-nc-nd/4.0/).

E-mail address: marinkc@umich.edu (M.K. Clark).

[★] This draft manuscript is distributed solely for purposes of scientific peer review. Its content is deliberative and predecisional, so it must not be disclosed or released by reviewers. Because the manuscript has not yet been approved for publication by the U.S. Geological Survey (USGS), it does not represent any official USGS finding or policy. Any use of trade, firm, or company names does not imply endorsement by the U.S. Government.

^{*} Corresponding author.

1. Introduction

Coseismic landslides have long been recognized as important secondary hazards of earthquakes in mountainous regions and potential contributors to mountain-scale erosional budgets (Keefer, 1994, 2002; Dadson et al., 2004; Hovius et al., 2011; Parker et al., 2011; Li et al., 2014). Landslides associated with earthquakes can contribute substantially to loss of life (Marano et al., 2010; Petley, 2012). For example, about 20,000 of 100,000 fatalities caused by the 2008 M_w7.9 Wenchuan earthquake in China have been attributed directly to landsliding (Huang and Fan, 2013). The debris generated by the tens to even hundreds of thousands of landslides associated with large earthquakes is also a potentially significant sediment source. Thus, these events may play a key role in the erosional budgets of active mountain belts (Keefer, 1994; Parker et al., 2011; Hovius et al., 2011; Li et al., 2014; Wang et al., 2015), as well as in biogeochemical cycling during orogenesis (e.g., St-Onge and Hillaire-Marcel, 2001; Jin et al., 2015; Wang et al., 2016).

Several features of coseismic landslide distributions determine their role as hazards and as erosional agents, including (i) the landslide number, area, and volume (e.g., Keefer, 1994; Malamud et al., 2004; Marc et al., 2016); (ii) the location of landslides (e.g., Dai et al., 2011); (iii) their mobility, i.e., the reach or horizontal runout distance of a failed mass, typically relative to its fall height or volume (e.g., Heim, 1932; Hsu, 1975; Davies, 1982; Dade and Huppert, 1998; Legros, 2002), and (iv) their connectivity, i.e., the extent to which landslide debris directly enters fluvial channels (e.g., Dadson et al., 2004; Meunier et al., 2007; Li et al., 2016). Despite a growing literature on earthquake-triggered landslides, the relative rarity of large earthquakes limits the available data and thus the scope for building and testing models predicting landslide magnitudes, locations, mobility, and connectivity. The April 2015 M_w7.8 Gorkha earthquake in Nepal offers a wealth of new information for understanding coseismic landslides. In this paper, we present a high-resolution map of Gorkha-triggered landslides and explore the implications of this inventory for understanding some of the fundamental characteristics of coseismic landslides. Specifically, we report the number, area, and estimated volume of landslides associated with the Gorkha event with a polygon inventory, meaning the area extent of individual landslides are mapped, and we assess how these values compare to inventories from previous earthquakes. The Gorkha inventory statistics provide a framework from which we speculate on the causative parameters determining landslide locations, which may explain how and why landslide density varied spatially during this earthquake. Finally, we evaluate both the mobility of Gorkha-induced landslides in light of past studies and theoretical expectations, and the connectivity between landslide debris and the fluvial channel system. Landslide mobility may influence connectivity, with implications for how landslides affect sediment dynamics (cf. Li et al., 2016), but such links have not been evaluated directly

Landslide mobility in particular has received less attention in prior work on earthquake-triggered landslides compared to other (e.g., rainfall-triggered) landslide events. Yet mobility directly relates to potential societal impact because with increasing travel distance, landslides are more likely to affect population centers and infrastructure and to dam rivers. Landslide mobility also modulates the influence of coseismic landsliding on sediment dynamics because longer travel distances are also expected to mean greater coupling between hillslope and fluvial systems. Most mobility studies have focused on relatively few, isolated large landslide events, such as the tragic 2014 Oso landslide (Iverson et al., 2015). With a few exceptions (e.g., Finlay et al., 1999; Qi et al., 2011; Guo et al., 2014), little prior work has assessed mobility in datasets of smaller landslides (<10⁶ m³ volume). To our knowledge, analysis of mobility for an entire coseismic landslide inventory has not been previously presented, though some studies have considered more restricted case studies of earthquake-associated failures (Qi et al., 2011; Zhang et al., 2013; Guo et al., 2014). The Gorkha event provides an opportunity to investigate the mobility characteristics of a large, statistically robust population of smaller landslides. By focusing attention on mobility of the Gorkha dataset, we hope to answer questions about the similarities and differences in mobility of small versus large volume failures, contribute to understanding dominant factors affecting horizontal travel length or reach, and assess how mobility relates to the connectivity of landslide debris with fluvial channels, and thus long-term sediment-related hazards.

1.1. Background: the 2015 $M_{\rm w}$ 7.8 Gorkha earthquake sequence and associated landslide event

The Himalayan front has long been recognized as an area of high seismic hazard (e.g., Molnar and Deng, 1984; Wesnousky et al., 1999; Bilham, 2004; Bollinger et al., 2014). Active continental convergence of India and Asia occurs at a rate of about 45 mm/yr (Sella et al., 2002), of which 20 mm/yr is accommodated by the seismogenic Main Himalayan Thrust (Lavé and Avouac, 2000). Earthquakes on this fault have included probable M9 events in the past, such as a large earthquake in 1505 (Bilham, 2004). However, only M8 earthquakes and smaller have occurred in Nepal in the last century, including the 1934 M_w~8 Bihar-Nepal quake (Bilham, 2004).

The Himalayan front is also recognized as a region of unusually high landslide hazard, particularly during the rainy summer monsoon season (e.g., Gerrard and Gardner, 2000; Petley et al., 2007; Korup et al., 2010). Steep topographic relief, intense precipitation, and high population density combine with the seismic potential to produce frequent fatal landsliding. Most non-seismic landslides occur during the summer months when heavy monsoon rainstorms destabilize slopes and trigger failures (Petley, 2012). Heavy landsliding in association with past earth-quakes has been described along the Himalayan thrust, including during the 1934 M_w~8 Bihar-Nepal quake (Pandey and Molnar, 1988), the 1950 M_w8.5 Assam quake (Mathur, 1953), and the 2005 M_w7.6 Kashmir quake (Owen et al., 2008), and supply of sediment from earthquake-triggered landslides in medieval times catastrophically clogged river valleys in central Nepal (Schwanghart et al., 2016).

The 25 April 2015 M_w 7.8 Gorkha event ruptured a ~140 km long, east-west segment of the Main Himalayan Thrust (MHT) but did not produce a surface break (Fig. 1; Hayes et al., 2015). The rupture initiated near Barpak, ~80 km northwest of Kathmandu, and propagated eastward. The event was followed by a series of large aftershocks, including a M_w 7.2 event on 12 May which ruptured a portion of the MHT directly east of the 25 April rupture (Avouac et al., 2015). Nearly nine thousand deaths and economic losses equivalent to billions of US dollars resulted from the mainshock alone (Zhao, 2015). Due to the magnitude of the event and the proximity of the rupture plane to the surface, extensive landsliding was anticipated from this earthquake.

Immediately after the event, various international groups began working to identify landslides triggered by the quake for disaster-relief and early scientific purposes (British Geological Survey, 2015; ICIMOD, 2015; Kargel et al., 2016). Early reports of landslide numbers (e.g., n = 4312; Kargel et al., 2016) were lower than expected for the moment magnitude of the earthquake (e.g., compared to the >10.000 landslides expected for an earthquake of this magnitude based on statistical relationships between landslide event magnitude and moment magnitude for shallow crustal earthquakes; Malamud et al., 2004). However, early field evaluation suggested that number would rise to a few tens of thousands with more detailed investigations (Collins and Jibson, 2015). More than 69 landslide dams were formed, which temporarily, fully, or partially blocked rivers and posed threats to populations downstream (Collins and Jibson, 2015).

2. Methods

High-resolution, high-quality satellite imagery collected weeks to a few months after the Gorkha event enabled mapping of coseismic

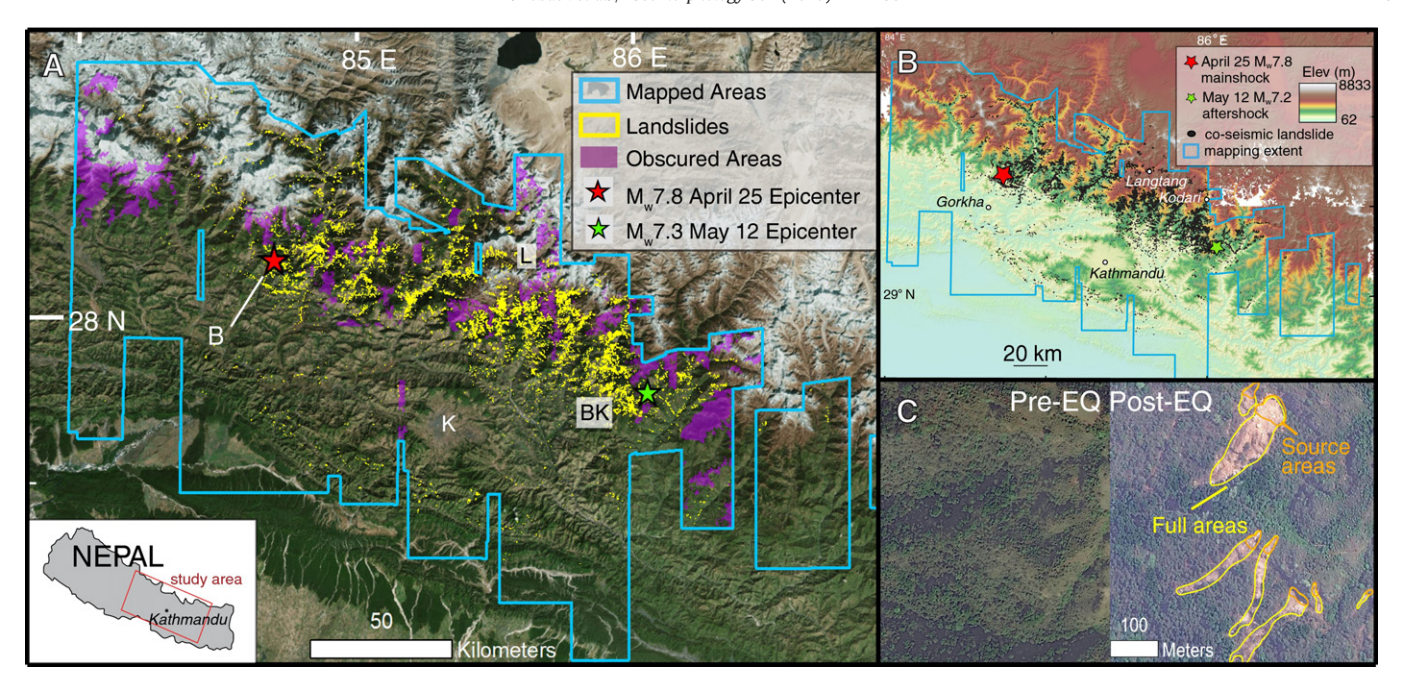


Fig. 1. Landslide inventory. A) Satellite image of central Nepal showing landslides related to the April–May 2015 Gorkha earthquake sequence (UTM projection with WGS 1984 datum). B = Barpak, K = Kathmandu, BK = Bhote Kosi, L = Langtang. Obscured areas due to persistent cloud cover (purple) are excluded from density and area calculations. B) Landslide inventory relative to topography. C) Example of pre- and post-earthquake imagery used for identifying coseismic landslides located near the epicenter (Barpak). Source (orange) and full area (yellow) polygons of each landslide are differentiated.

landslides in detail (Figs. 1 and 2). We examined pre- and post-earthquake orthorectified and georeferenced images in order to visibly identify coseismic landslides (Fig. 1C). We were able to differentiate scar (source) areas and deposit (runout) areas, allowing us to create the first inventory for a complete coseismic landslide event that to our knowledge includes such delineation as polygons. This mapping superseded immediate response and recovery efforts comprised of point identification of landslide locations (Kargel et al., 2016) or lines along landslide long axes (Earthquakes Without Frontiers, 2015). In this study, closed polygons that follow the landslide perimeter and source area are determined in a GIS framework. Having polygons within a GIS framework permits analysis of topographic, climatic and seismic characteristics with the landslide inventory for source and full areas separately. Since the time of submission of this manuscript for publication, we have become aware of two other polygon-based inventories for this event reported in the scientific literature: a complete inventory from Martha et al. (2016), and a partial inventory (with landslides only $> 1000 \text{ km}^2 \text{ area}$) from Xu et al. (2016).

Following identification of landslides in plain view, we calculated geospatial statistics using ~30 m horizontal resolution digital topography data derived from the Shuttle Radar Topography Mission, i.e., SRTM data (Farr et al., 2007). The 30 m SRTM data for Nepal includes large holes in some areas, but these were mostly outside of the region of landslide mapping in this study. However, routine void filling using the ArcGIS void filling tool was completed prior to analysis.

2.1. Landslide mapping from satellite imagery

Coseismic landslides were mapped by comparing pre- and postevent high-resolution satellite photographs (Fig. 1C; data archived with the USGS as Roback et al., 2017). We primarily used DigitalGlobe Worldview-2 and -3 imagery, supplemented with Astrium's Pleiades satellite data and imagery sourced from Google Earth where the Digital Globe data was cloud-covered or distorted. Resolution of imagery (ground sample distance) used in our mapping is 20–50 cm in most areas. Acquisition dates of imagery used to map landslides ranged from 26 April to 15 June 2015, with most images collected between 2 May and 8 May 2015 (Fig. 3B). Because few cloud-free images were available in the first week following the mainshock, it is possible that some mapped landslides may have been triggered by large aftershocks or by rainfall. When multiple sets of imagery from different dates were available for an area, the imagery which was least distorted was used to map the outline of landslide sources and deposits, and earlier imagery was used to confirm the earliest date that the landslide could be recognized. Areas obscured by clouds, steep terrain, or severely distorted imagery were excluded from the statistical calculations and indicated as such with closed polygon regions (Fig. 1, Roback et al., 2017). These areas are identified in Fig. 1. We attempted to identify landslides associated only with the main shock on 25 April, but in some cases imagery was not available until after the 12 May M_w7.2 aftershock (this affected 3349 of 24,915 total mapped landslides). Rarely, some other areas, accounting for 1752 landslides, required use of postmonsoon imagery to define the landslide polygon extent (i.e., collected after 15 June), and in these cases, identification of the landslide as postearthquake/pre-monsoon and the approximate pre-monsoon size were verified from distorted or cloudy pre-monsoon imagery.

The high quality imagery available for this event allowed us to recognize landslides as small as a few tens of square meters and to delineate landslide source from the full landslide area. Pansharpened and orthorectified visible-light and panchromatic images were assessed for visible changes in land cover or texture and outlined manually onto the georeferenced imagery. Small landslides were recognized by changes in reflectivity due to surface disruption or loss of vegetative cover, and larger landslides were identified by the fresh appearance of morphologic features (i.e. scarp, toe, lateral margin). Source areas were delineated by recognition of the headscarp, which usually formed a circular or oval depression at the uppermost part of the landslide, and exposed landslide scar. Distinction between source (i.e. landslide scar) and deposit areas were recognized based on textural differences, especially where exposed rock versus debris could be recognized as such. Source areas are minimum areas because debris often obscured the lower slip surface and debris transport likely also included some amount of entrainment. However, we acknowledge that such distinction can be uncertain and the uncertainties difficult to quantify. Fresh

landslides were most easily recognized by the changes in spectra associated with vegetation loss but were generally more difficult to recognize above treeline. At these higher elevations, landslides were easily observed where fresh deposits overlaid snow but otherwise were identified by more subtle changes in reflectivity or morphology of bedrock surfaces. The difficulty in identifying landslides in areas without vegetation or snow may bias observations toward minimum estimates of landsliding in these settings.

Combining adjacent landslides into single polygon features, or "amalgamation," is known to skew landslide inventory statistics by overestimating the total volume affected by landsliding and increasing or decreasing the number of large and small landslides respectively (Li et al., 2014; Marc and Hovius, 2015). In order to minimize such effects, adjacent landslides with separate source areas were mapped as separate polygons to the greatest extent possible. Where deposits from multiple source areas joined, the deposit area below the converging point

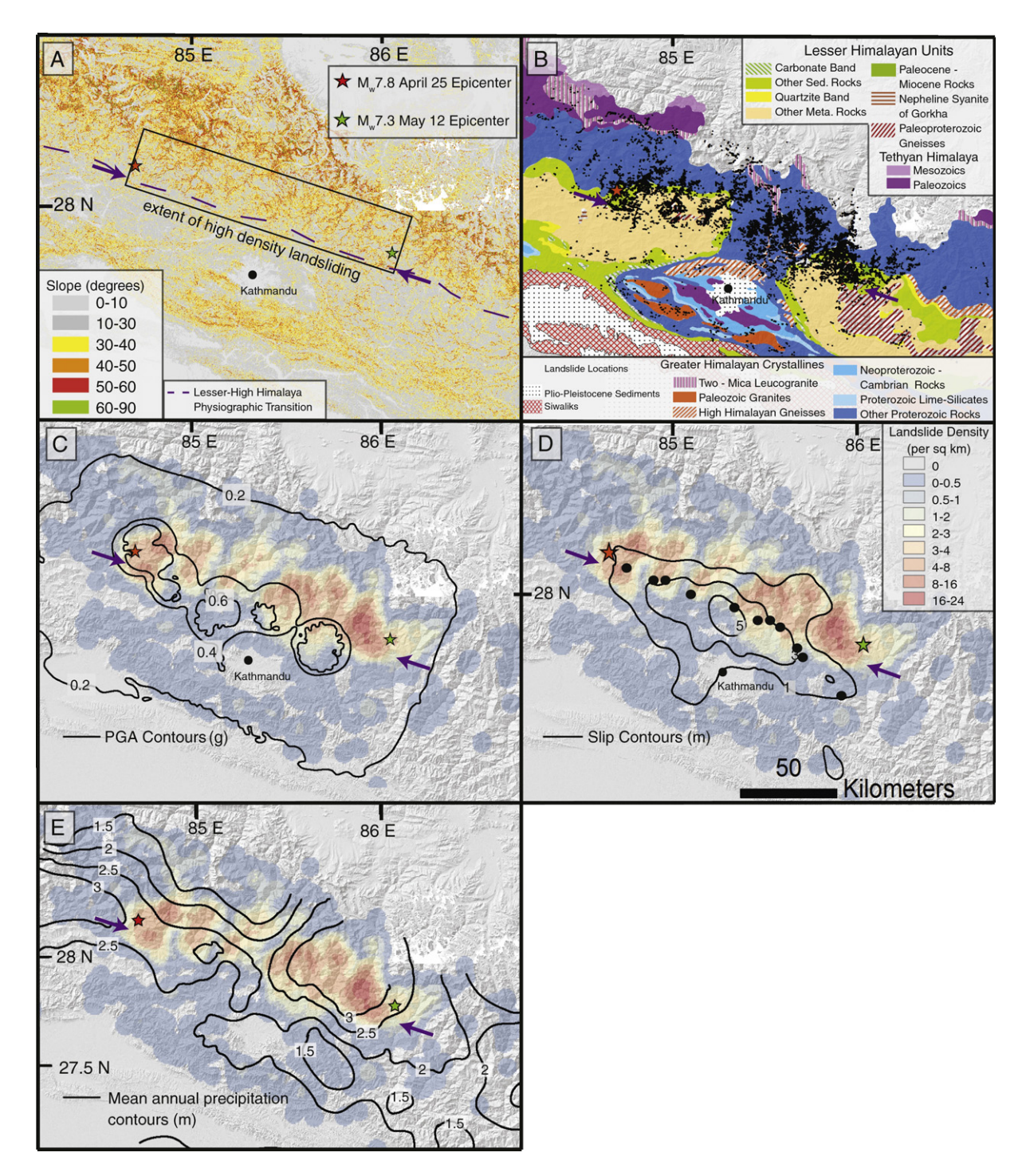


Fig. 2. Landslide inventory relative to topographic slope, geology, ground shaking and finite fault slip. Purple dashed line or purple arrows indicate a NW-SE line along which slopes dramatically steepen, marking the change from the Middle Hills/Lesser Himalaya to the High Himalaya. A) Topographic slope derived from SRTM digital topography (30 m resolution). Note dramatic steepening of topography northeast of the "physiographic transition". B) Major geologic units of central Nepal (Dhital, 2015). C-E) Landslide density (color) compared to: C) peak ground acceleration from the USGS ShakeMap model v.9 (July 2015); D) surface projection of modeled finite fault slip (Galetzka et al., 2015), with circles representing the source location of 0.5–2 Hz energy (Galetzka et al., 2015; Avouac et al., 2015); E) contours of mean annual precipitation, derived from reanalyzed TRMM 2B31 data (Bookhagen and Burbank, 2010).

was assigned only to the largest contributing source area to prevent double counting of deposit areas in the inventory. In some cases, branched runout areas were identified from a unique source area and were mapped as a single polygon.

2.2. Data sources used for calculating landslide statistics

The elevation and slope of landslide polygons were derived from 1 arc sec, or ~30 m horizontal resolution, SRTM digital topography (Fig. 2; Farr et al., 2007). Slope statistics include the maximum slope and mean slope from pixels within the full-area polygon for each landslide. While the high-resolution imagery enabled mapping of many small (<100 m²) landslides, precise characterizations of elevation and particularly slope was not possible for such small features because of the relatively coarse resolution of the DEM.

Estimated PGA from the 25 April main shock was calculated for each landslide feature using the latest version of the USGS ShakeMap for that event (v9, released 2 July 2015). ShakeMap estimates are based on ground motion attenuation equations constrained by instrumental strong ground motion records and felt/damage reports where they exist (Earle et al., 2009). Due to a paucity of felt reports and direct measurements across the study area, the ShakeMap PGA for this event is poorly constrained ("Grade C"). Modeled finite fault slip estimates were derived from Galetzka et al., 2015 (Fig. 2). Mean annual precipitation data were taken from TRMM 2B31 reanalysis (Bookhagen and Burbank, 2010), which provides sufficiently high-resolution estimates to discern spatial trends at the scale relevant to this study (unlike TRMM 3B41 or APHRODITE data; cf. Andermann et al., 2011). Information on the distribution of geologic units in Nepal was collected from Dhital (2015).

Landslide volume (V), area (A), runout length (L), and height drop of the landslide mass (H) (i.e. elevation difference from the uppermost part of the source and the lowermost part of the deposit) were also calculated. Unless stated otherwise, landslide volume was calculated using a range of area-volume scaling relations, as detailed below. Runout length was estimated using a simplified polygon enclosure of the mapped landslides from which the length of the long and short axes could be determined. Most Gorkha-induced landslides have long, narrow, and linear runout paths for which the long axis of the bounding polygon coincides with the runout path. Deviations from this geometry include landslides with source areas that align along short cliffs, in which case the runout length corresponds with the short axis instead. Also, sharp curves in the runout path can lead to underestimation of runout distance. For 38 landslides that were found to have anomalously high mobility via the automated calculation, runout length was corrected manually. The ratio between the runout length and height drop, sometimes referred to as the "angle of reach" or "fahrböschung angle," are typical measures of the mobility of the landslide (e.g., Heim, 1932; Hsu, 1975; Dade and Huppert, 1998; Iverson, 1997). Landslide runout length to height ratios (L/H) were determined only for landslides with source areas $> 10^3$ m², because smaller areas were subject to large height uncertainties due to the ~30 m DEM resolution.

2.3. Delineating fluvial channels and evaluating landslide-channel connectivity

To assess the extent to which landslide debris was delivered to the river systems of Nepal during the Gorkha earthquake, we evaluated the position of distal portions of landslides relative to stream channels ("landslide-channel connectivity"; Dadson et al., 2004; Huang and Montgomery, 2014; Li et al., 2016). We identified channelized portions of the landscape via inspection of satellite imagery and based on local gradient-upstream contributing area (G-A) relations. On a G-A plot, different geomorphic domains (i.e., hillslopes vs. channels) are typically characterized by power-law relations with different exponents (e.g., Montgomery and Foufoula-Georgiou, 1993; Montgomery and

Buffington, 1997; Sklar and Dietrich, 1998; Montgomery, 2001). We plotted a region-wide G-A relationship for the area covered by landslide mapping by calculating the mean slope angle, or gradient (G), for increments of upstream drainage area (A) determined using ArcGIS flow routing algorithms (we used 0.1 log unit increments of A in km²), in all cases using the 30 m SRTM DEM. Geomorphic domains were identified from this plot using a "pruning" approach (e.g., Stock and Dietrich, 2003; Densmore et al., 2007), i.e., successively adding larger upstream area data and repeatedly fitting a linear relation to the logarithmic G-A data until a local statistically optimal fit was achieved. Each domain is characterized by a locally optimized fit. With this approach, we identified the A values characteristic of (1) hillslopes, (2) valley heads, (3) colluvial channels, and (4) fluvial channels (including bedrock and alluvial channels), each with successively larger A.

We complemented the G-A approach by evaluating the A value at the locations where visibly identifiable channels begin, based on inspection of the satellite images used for landslide mapping (channels were visibly distinguished by absence of vegetation and distinctive morphology). We describe this as the threshold for initiation of "visually identifiable channels."

Landslide-channel connectivity was evaluated using two approaches based on raster data and vector data, respectively. For the raster-based method, the maximum upstream area (A_{max}) within the extent of the landslide polygon was derived for each landslide and compared to the threshold area (A_c) for channels. If $A_{max} > A_c$, the landslide was determined as connected to channels, and vice versa. This approach may miss landslides that actually intersect channels (underestimating connectivity) if channels are wider than the 30 m DEM resolution and in other cases may incorrectly identify landslides as channel-connected due to the simplified geometry of mapped channels. For the vector-based method, all cells with area values $> A_c$ were converted to linear features with a buffer zone of width ranging from 50 m to 400 m. Landslide polygons intersecting with the channel buffer zones were identified as channel-connected.

3. Results

3.1. Landslide number, volume, and area-frequency statistics

We have identified 24,915 landslides with a total area of 87 km². Because some regions of Nepal have remained shrouded by continuous cloud cover in all available imagery since the earthquake (as of the completion of our mapping in July 2016), these areas could contain additional landslides. However, these obscured areas account for only ~10% of the total region affected by landslides and are largely confined to regions at high elevation where we assume landslide occurrence was low based on the low landslide densities in nearby areas of similar elevation. The distal portions of the mapped region also have low landslide densities, so while we expect that some landslides occurred at distances beyond our mapped region, the total number of unmapped slides is likely small relative to the mapped total.

We estimated total landslide volume (V) using a power-law landslide area-volume scaling relationship: $V = \alpha A^{\gamma}$, where α and γ are empirically-calibrated scaling parameters and A is the full landslide area. We considered a range of different parameter combinations determined from global data compilations, including those specific to the Himalaya (Table 1). We calculated volume for each individual landslide using this relation and summed these values across the entire mapped inventory. The resulting estimates of total volume associated with Gorkhatriggered landslides range from 0.12 to 1.1 km³ (Table 1). The scaling parameters for mixed soil and bedrock landslides in the Himalaya from Larsen et al., 2010, yield a total volume estimate of 0.81 + 0.11/-0.09 km³ (one-sigma range from Monte Carlo error propagation considering reported uncertainties in scaling parameters). The wide range in total volume estimates underscores the need for more accurate determination of total volume associated with the Gorkha-

Table 1Gorkha-triggered landslide volumes estimated using different scaling parameters.

Scaling parameters	$\log_{10}(lpha)$	γ	V (km ³)
Himalayan mixed soil & bedrocka	-0.59 ± 0.03	1.36 ± 0.01	0.81 + 0.11 / -0.10
Himalayan bedrock ^a	-0.49 ± 0.08	1.34 ± 0.02	0.83 + 0.27 / -0.21
Global soil (full area) ^a	-0.44 ± 0.02	1.145 ± 0.008	0.13 + 0.01 / -0.01
Global soil (scar area) ^a	-0.65 ± 0.02	1.262 ± 0.009	0.26 + 0.28 / -0.25
Global bedrock (full area) ^a	-0.73 ± 0.06	1.35 ± 0.01	0.53 + 0.10 / -0.08
Global bedrock (scar area) ^a	-0.63 ± 0.06	1.41 ± 0.02	1.27 + 0.36 / -0.28
Global mixed (full area) ^b	- 1.1308	1.45 ± 0.0086	0.62 + 0.62 / -0.56

Volume calculated by the relation $V = \alpha A^{\gamma}$ and reported as median \pm ranges from 16th and 84th percentiles of 10,000 times Monte Carlo sampling for each group of parameters. Global soil and bedrock scaling for scar areas were applied only to source areas. Other scaling used the full landslide areas of the Gorkha inventory.

earthquake, which will most likely be based on local calibration of the area-volume relationship.

Power-law scaling of landslide area distributions is a typical characteristic of moderate to large landslides in most inventories (Hoyius et al., 1997; Stark and Hovius, 2001; Malamud et al., 2004). We examined the area-frequency distribution of the Gorkha event by log-binning a normalized, non-cumulative size-frequency distribution, allowing us to plot frequency-density (f = dN/dA, where N refers to the number of landslides in each bin) as a function of binned landslide area (A + dA)(Fig. 3A). Landslide frequency for the smallest landslides is typically undersampled and is dependent on the resolution of the images used for mapping, making interpretation of this relationship at low values of A difficult (Stark and Hovius, 2001). For the Gorkha event, landslides $> 10^4$ m² exhibit a power-law scaling with an exponent β of -2.5 (Fig. 3A). This value is higher than exponents reported for other coseismic inventories (Northridge, California = -2.39; Chi Chi, Taiwan = -2.30; Wenchuan, China = -2.19; Crosta et al., 2014) and also higher than the average of event-based and historical inventories $(\beta = -2.3)$ reported by Van den Eeckhaut et al., 2007. The higher value may reflect greater ability to recognize smaller landslides in high quality imagery, the relative lack of large landslides in the Gorkha event, or our attempts to divide areas of adjacent landsliding into individual slides rather than larger amalgamated complexes. An explanation based on fewer large landslides in the Gorkha event is supported by field observations (Collins and Jibson, 2015). The less steep powerlaw slope (-2.2) found for landslides from the Langtang region (Lacroix, 2016) may reflect local prevalence of larger landslides; for example differences in topography between fluvial versus glacial landscapes may set the upper limit on potential landslide size (Gallen et al., 2015). Differences may also result from mapping techniques, mainly the use of DEM differencing (Lacroix, 2016) versus manual identification from satellite imagery (this study).

3.2. Landslide density: first-order patterns

In accord with the observations made by Kargel et al. (2016), we find that landsliding associated with the Gorkha earthquake was mainly concentrated in the metamorphic Lesser and Greater Himalayan rock sequences and located preferentially in the steep topography of the High Himalaya (Figs. 2, 4). Relatively few landslides were identified in the moderately steep, lower elevation ranges that surround Kathmandu Basin. Landslide occurrence abruptly increases across the transition from moderate slopes of the Lesser Himalaya/Middle Hills to the steeper slopes of the High Himalaya, across the so-called "physiographic transition" (Fig. 2A; e.g., Wobus et al., 2003). This transition is also marked by high mean annual precipitation (MAP; Fig. 2B).

The Gorkha inventory also shows a generally eastward-directed increase in landslide density (Fig. 5B). A peak in landslide density occurs near the epicentral region; landslide density then decreases east of the epicenter before again increasing toward the eastward end of the rupture area. The highest peak in landslide density occurs just east of the termination of the mainshock rupture, corresponding to the Bhote Kosi river area (Figs. 1, 2, 5). Landslide density decreases more rapidly to the west than the east of the epicentral region. Based on our mapping with immediately post-seismic images (most collected between 2 and 8 May), the east-to-west trend likely predates the 12 May $\rm M_w 7.2$ aftershock located at the eastern terminus of the main shock rupture area (Figs. 1, 3B).

Comparison of imagery sets collected on 3 and 25 May over the highest-density areas of landsliding in the Bhote Kosi suggests that the

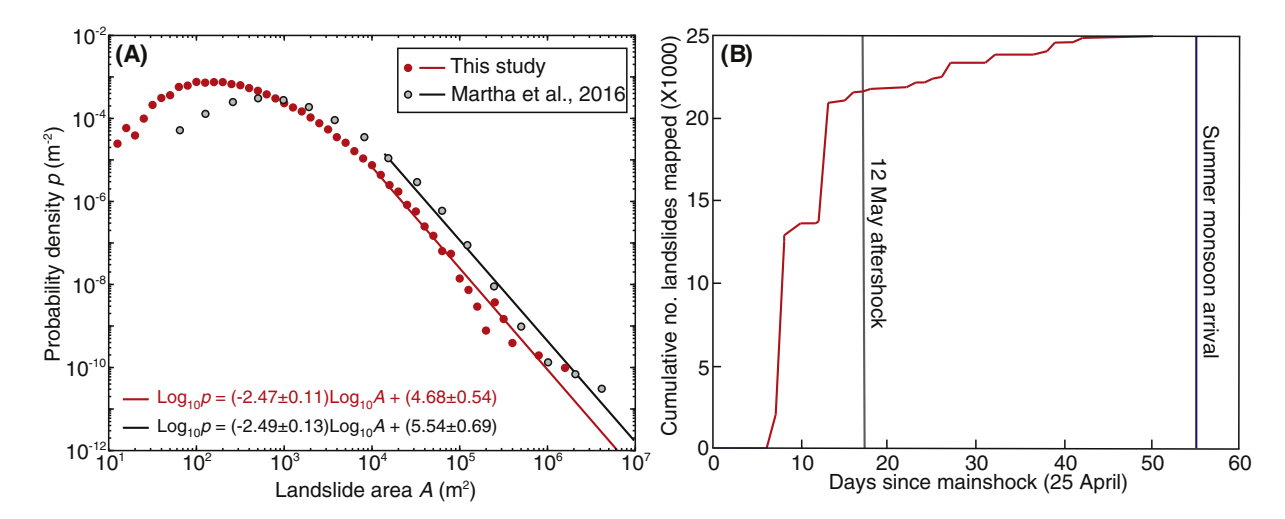


Fig. 3. Probability statistics and time series of the landslide inventory. A) Probability density-area statistics for the Gorkha landslide inventory calculated from the inventory presented in this paper and from Martha et al. (2016). Best-fit power-law function to the heavy tail of the distribution has a slope of -2.5 for both inventories. B) Cumulative number of landslides mapped as a function of time after the main shock.

a Larsen et al., 2010.

^b Guzzetti et al., 2009.

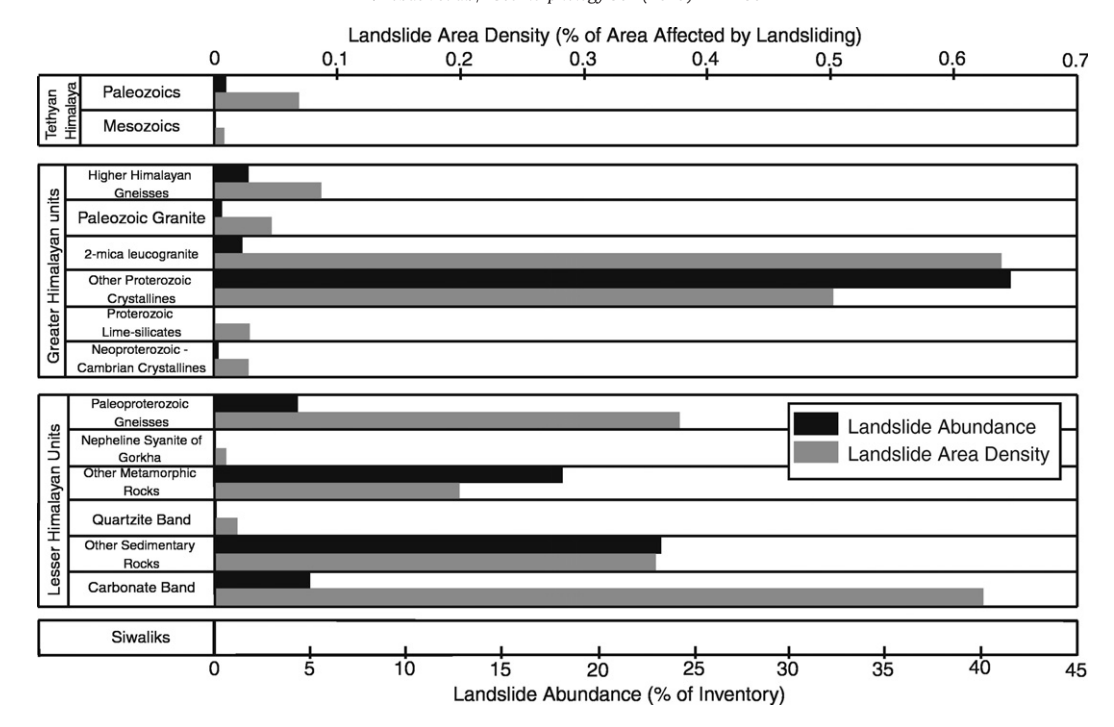


Fig. 4. Distribution of landslide frequency and percent area of landsliding by geologic units shown in Fig. 2B (Dhital, 2015).

M_w7.2 aftershock triggered only a small number of new landslides. We suggest that the 25 April mainshock effectively cleared most unstable material off of hillslopes in this area, leaving little weak material on the hillslopes when the large 12 May aftershock occurred. The eastward directivity of the main shock rupture may explain the intensity of landsliding in this area. Because the area was cloud covered between 25 April and 3 May, we cannot assess the role of smaller aftershocks, which may have preceded the 12 May event, in causing landslides. However, it is unlikely that such small earthquakes would have generated strong enough ground motions to initiate a large number of landslides because total energy release is dominated by the main shock and few landslides are generally observed for earthquakes below M4-5 (Malamud et al., 2004; Keefer, 1994; Marc et al., 2016). Although

our data allow preliminary evaluation, rigorously quantifying the full effect of aftershocks on landslide density in the Bhote Kosi region will require more detailed time series of landslide generation, for example based on detailed mapping of individual landslides using pre- and post-aftershock imagery.

3.3. Landslide density: relation to lithology, PGA, and slope

We do not observe a concentration of landsliding in any particular geologic unit at a regional scale (Figs. 2B, 4). In particular, curvature in the trace of the Main Central Thrust and Kathmandu Nappe leads to an equal areal distribution of the Greater and Lesser Himalayan rock units exposed throughout the earthquake-affected region (Fig. 2B).

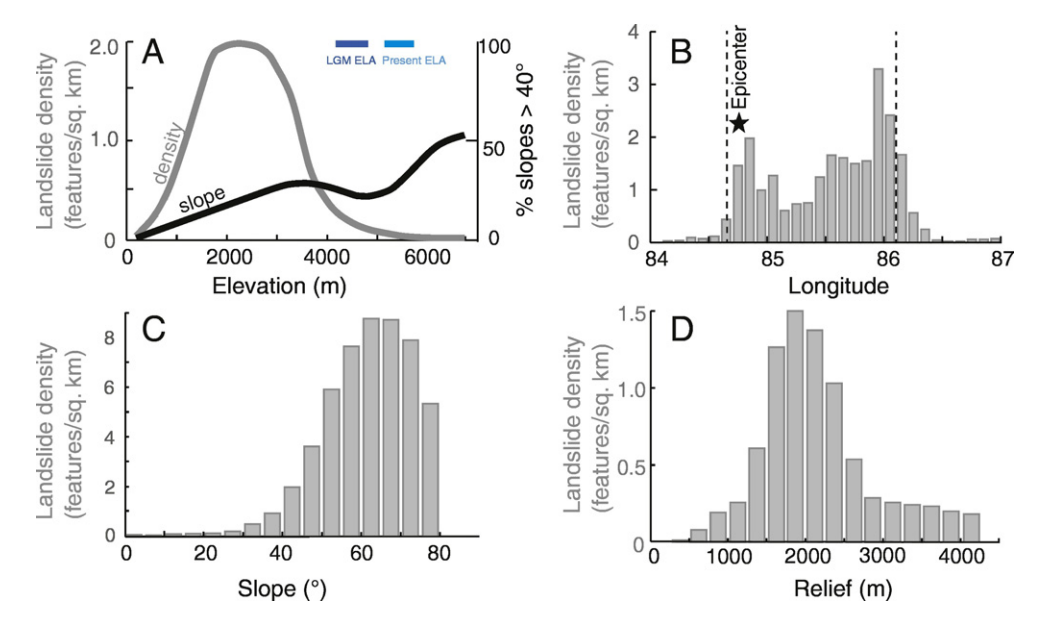


Fig. 5. Landslide inventory statistics. A) Distribution of landslide density (grey) and the percentage of steep slopes (>40°) (black) as a function of elevation. Elevation intervals of the glacial equilibrium-line altitude (ELA) for the present time and the last glacial maximum (LGM) are shown in blue. B) Landslide density as a function of longitude. C) Landslide density as a function of topographic slope. D) Landslide density as a function of relief calculated over a 2.5 km circular moving window.

We observe an even distribution of landslides between units of these two major lithologic sequences, which both comprise variably metamorphosed sedimentary and igneous rocks and are thought to be characterized by similar bedrock erodibility (Lavé and Avouac, 2001; Craddock et al., 2007) (Fig. 4). Within these units, the highest landslide abundance is within the most general map units that encompass large areas (i.e., "Other Proterozoic Crystalline" in the Greater Himalaya, and "Other Metamorphic" and "Other Sedimentary" in the Lesser Himalaya). Locally, some units have a high percent of landslide area (i.e., 0.7% of the area of the Greater Himalayan two-mica leucogranite is covered by slides; Figs. 2B, 4). These sub-units have restricted geographic exposure and happen to occur in regions of high-density landsliding in the epicentral region (near Barpak) and the Bhote Kosi river valley (locations noted on Fig. 1; also see Fig. 2B). We also do not observe abrupt changes in landslide density near mapped lithologic contacts, which might otherwise indicate lithologic control on landslide occurrence.

The landslide density from the Gorkha earthquake does not correlate directly with modeled PGA or with the surface projection of the highest slip from modeled GPS and teleseismic back projections in the northsouth direction, although density does more closely follow the extent of rupture and PGA > 0.1 g in the roughly E-W direction (Fig. 6). Except for the localized region around the epicenter of the 25 April main shock, high density landsliding occurs at relatively low values of modeled PGA (mostly 0.2–0.3 g), while moderately steep topography overlies regions of much higher modeled PGA along the Middle Hills and ranges south of Kathmandu Basin (0.6–0.8 g). Slip occurred on a shallow thrust fault plane beneath the Kathmandu Basin and partly along the transition to the deeper, steep portion of the Main Himalayan Thrust (MHT). Less than 50% of the landslides are located within the region defined by the surface projection of the >1 m slip contour (Galetzka et al., 2015), a proxy for distance to the rupture (Figs. 2D, 6). The remainder of landslides is mostly present at greater distances north and northeast of the rupture area, concentrated above the deepest portion of the fault plane (Ader et al., 2012) that ruptured in this event (Fig. 2C and D).

Landslide density is also not a simple function of slope or precipitation; for example, the steepest slopes in the High Himalaya are not characterized by the highest landslide density, and landslide density is low where precipitation is high in the Middle Hills (Figs. 5, 6). Thus, in summary, we do not observe a single control on the distribution of landslide

density associated with this event. In the Discussion section, we consider how a confluence of factors may have determined landslide occurrence.

3.4. Source area characteristics

The characteristics of landslide source areas are important for evaluating mobility (discussed below) and may shed light on how different landscapes (e.g., vegetated vs. glacial) affect failure mode. Our ability to distinguish source areas in the high-resolution imagery used in this study provides a rare view of landslide source area characteristics for a coseismic inventory. Gorkha landslide sources are typically small compared to the total landslide area and range from $<10 \text{ m}^2$ to $>10^5 \text{ m}^2$. The small source areas are typically above long, narrow runout areas and deposits. Mean source area size increases with elevation across the study area (from mean elevation bins of 250 to 5750 m; Fig. 7A). Mean source area size is uniform for slides with maximum slopes less than ~40° and increases with increasing maximum slope above this value (Fig. 7B). The trend of source area size with mean slope is similar to that with maximum slope, namely increasing area with increasing slope, although the correlation is not as strong and landslide source area appears to decline at the steepest mean slopes (Fig. 7C). The association of larger landslides with higher elevations and steeper slopes may reflect the longer, steeper hillslopes observed in the glaciated terrain and greater potential for producing deep-seated landslides, compared to smaller, shallower landslides observed at lower elevations on densely vegetated slopes. In general, relief, mean slope, and elevation are strongly coupled in the Nepal Himalaya (Gabet et al., 2004), suggesting that larger source areas are probably also related to greater relief and longer hillslope lengths.

3.5. Mobility indices of Gorkha-triggered landslides

Mobility describes the runout characteristics of a landslide, often evaluated in terms of volume, height drop, and/or topographic slope (e.g., Heim, 1932; Kent, 1966; Hsu, 1975; Dade and Huppert, 1998; Finlay et al., 1999; Hunter and Fell, 2003; Iverson et al., 2015). We analyze mobility by three measures: (1) runout length as a function of slope and volume, (2) source area to full mapped area ratios (S/F), and (3)

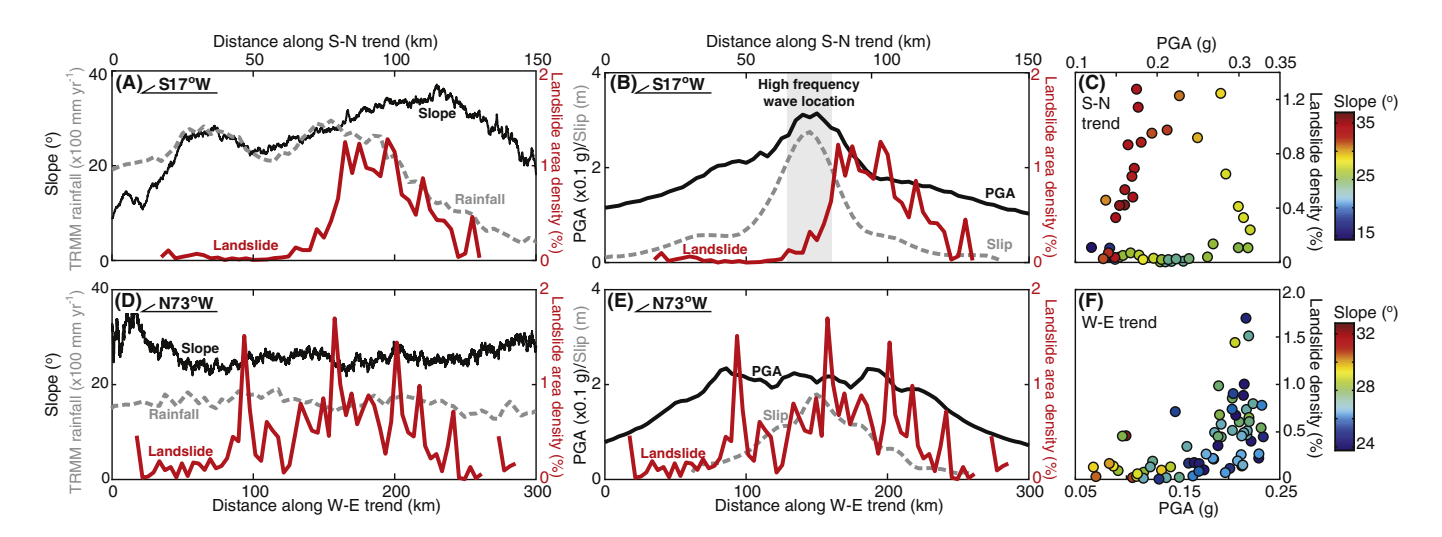


Fig. 6. Swath profiles of landslide density and metrics of topography, climate, and seismotectonics; and relations between landslides and PGA and slope. A–B) Swath profiles across the trend perpendicular to the fault strike (approximately south to north), showing 2 km-wide incremental averages of: A) landslide area density (red curve), rainfall (1998–2009 TRMM-derived MAP, grey dashed curve), and slope (black curve, from SRTM 30 data); B) landslide area density (red curve), modeled PGA (black curve), and seismic slip (grey dashed curve); the grey band indicates the locations of 0.5–2 Hz seismic energy sources. C) Cross-plot of mean values of PGA and landslide density within each increment (each 2 km width) along the N–S swath profile. Color-coding is mean slope angle within each increment. D-E) Swath profiles across the trend parallel to the fault strike (approximately west to east), showing 4 km-wide incremental averages of E) landslide area density (red curve), rainfall (grey dashed curve) and slope (black curve); F) landslide area density (red curve), slip (grey dashed curve) and PGA (black curve). F) Cross plot of mean values of landslide area density vs. PGA as in C) but for each 4-km increment along the E-W profile.

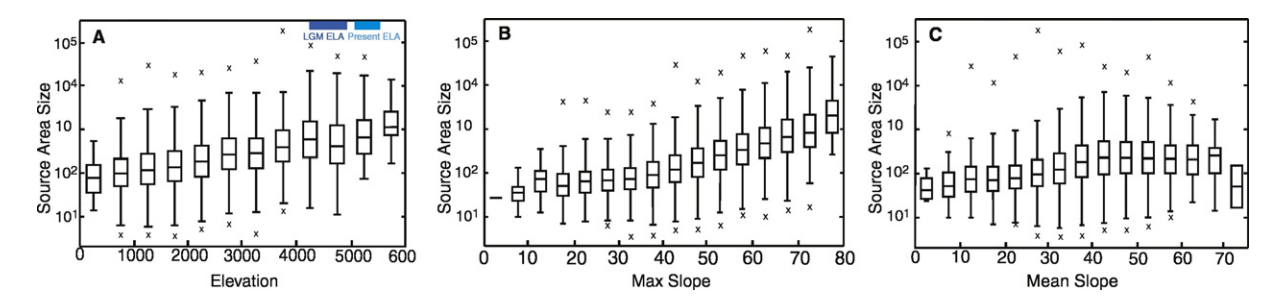


Fig. 7. Landslide source area statistics. For each box, the central mark indicates the median, and the bottom and top edges of the box indicate the 25th and 75th percentiles, respectively. The whiskers extend to the most extreme data points not considered outliers, and the outliers are plotted individually using the "x" symbol. A) Source area size as a function of elevation. Elevation intervals of the glacial equilibrium-line altitude (ELA) for the present time and the last glacial maximum (LGM) are shown in blue. B) Source area size as a function of the maximum slope for full landslide areas. C) Source area size as a function of the mean slope for full landslide areas.

runout length to height drop ratios (L/H). The first two measures provide estimates of landslide spreading, i.e., how a landslide volume is distributed both downslope and laterally spread across the slope, which has been argued to be the main controlling factor on landslide runout (e.g., Davies, 1982; Legros, 2002). The latter measure, the ratio of height drop to runout length (Heim, 1932), has been suggested to represent the frictional characteristics of a landslide mass and the surface it overrides; ratios observed for small landslides (<10⁵ m³) match those predicted from purely frictional slides (e.g., Shreve, 1966; Scheidegger, 1973; Hsu, 1975; Corominas, 1996). The physical meaning of this ratio has been debated (and questioned) for decades, and other observations suggest that average values may be modulated by topographic boundary conditions (e.g., Nicoletti and Sorriso-Valvo, 1991). Regardless, very mobile landslides in the historical record have unusual runout lengths over fairly gently sloping topography and can be identified by

high L/H ratios (e.g., Dade and Huppert, 1998). These slides have L/H ratios generally > 2, with ratios of 5 to 10 observed for several well-studied examples in the historical record. For example, the 2014 Oso, Washington, USA landslide had a value of approximately 10 (Iverson et al., 2015).

As expected, larger landslides in the Gorkha inventory have greater potential energy and thus have longer runout distances, ranging from more than a few hundred meters to a few kilometers for landslides larger than $10^3 \, \text{m}^2$ in area (Fig. 8). We observe that landslides that originate from steeper slopes also tend to be more mobile than those from shallower slopes on the basis that runout length increases with maximum slope within the landslide area, but this is largely a function of increasing landslide area (or volume) with increasing slope. Gorkhatriggered landslides follow a power-law scaling between landslide volume and runout length similar to data observed for subaerial landslides

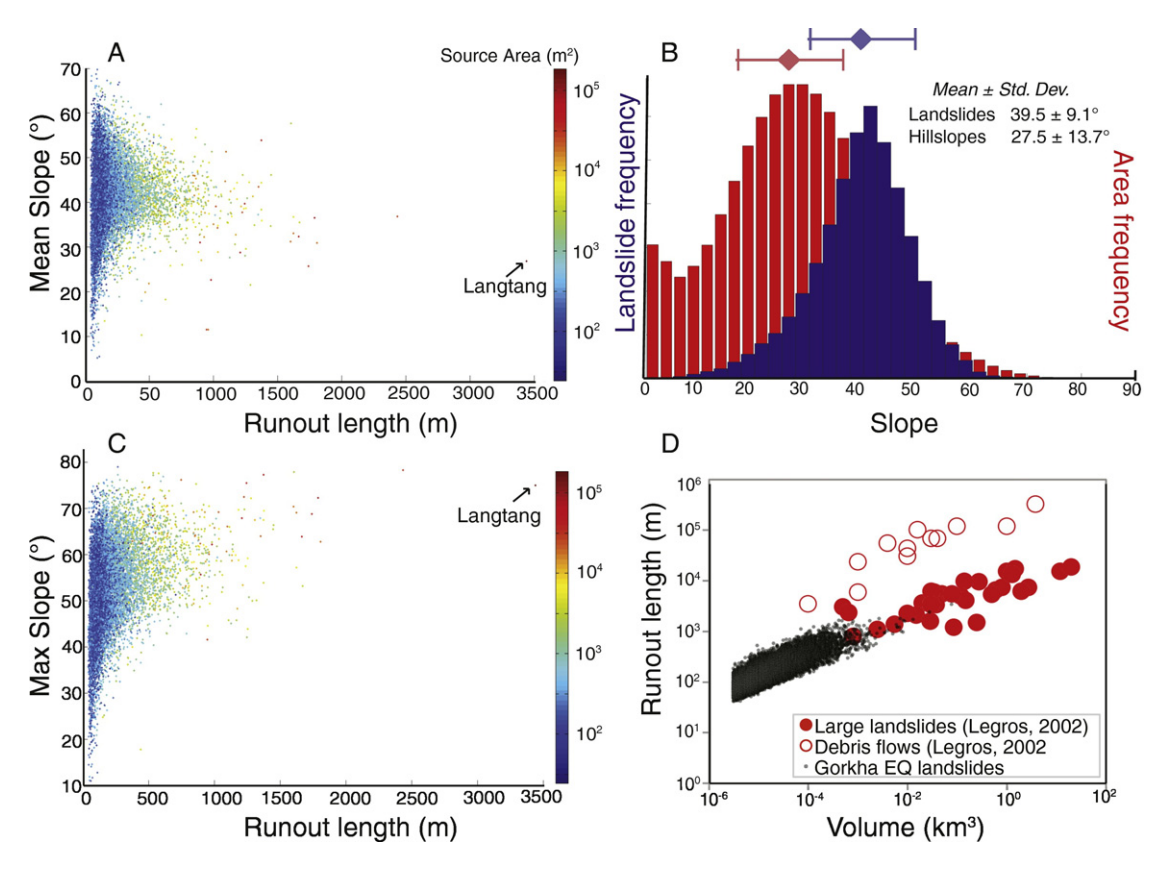


Fig. 8. Landslide area statistics relative to slope and runout length. A) Scatter plot of landslide source area size relative to mean slope and runout length. B) Histogram of mean slope for full landslide areas for the complete inventory compared to the entire landscape. Mean and maximum slope values are calculated within the full landslide polygons, which includes source, runout and deposit areas. C) Scatter plot of landslide source area relative to maximum slope and runout length. D) Comparison of runout length versus inferred landslide volume for the Gorkha inventory compared to published landslide compilations (Legros, 2002).

in the global compilation of Legros (2002) (Fig. 8D). This compilation focused on much larger failures; by including the Gorkha data, we find that the consistent runout-volume relationship extends over >6 orders of magnitude. In contrast, subaerial debris flows from the Legros (2002) compilation plot at notably higher runout lengths relative to source volume, differing by as much as 2 orders of magnitude from subaerial landslides (Fig. 8D).

The average landslide source to full mapped area ratio (S/F) observed for landslides associated with the Gorkha earthquake is 0.17. In contrast, global S/F averages are ~0.34 for soil landslides and ~0.48 for bedrock landslides, calculated from volume-area scaling parameters (Larsen et al., 2010, supplementary data) assuming that the volume of landslide sources and deposits is the same, such that $A_d/A_s = (\alpha_s/\alpha_s)$ $(\alpha_d)^{1/\gamma}$ where s and d refer to scar and deposit, respectively, and that the full areas are the sum of scar and deposit areas. The low ratio for Gorkha earthquake-triggered landslides likely reflects topographic influences; the steep, long hillslopes of the Greater Himalaya enable source material to run out over long horizontal distances. While runout distance scales with landslide volume, the proportion of the two (i.e. the ratio of source to full landslide area) is nearly constant, and we observe a near linear relationship between the source area size and full area size (Fig. 9B). In support of this interpretation, scatter plots of S/F ratio versus mean and maximum slope show no systematic relationship between these variables (Fig. 9C and D). This tight relationship further supports the notion that debris runout, in terms of both area and distance, is primarily a function of source size, which is likely also coupled to hillslope length.

Subjective bias in distinguishing landslide source from runout areas could affect S/F ratios. However, the small size of landslide deposit areas observed for most landslides in satellite imagery from the Gorkha event corroborate the small mapped source areas with long transport distances. Field observations of long runout pathways lend further support to this interpretation. In cases where landslides traveled down perennial or ephemeral stream channels, water or overridden saturated

materials also may have played a role in transport distance. We have not undertaken identification of such features, but the Gorkha earth-quake occurred during low water conditions and at the end of the dry season in Nepal (Collins and Jibson, 2015). Based on the climatology leading up to the earthquake, we do not expect local hydrology to have contributed to runout distances because the near-surface ground conditions were likely unsaturated and ephemeral streams were dry. However, dynamic changes in the height of the water table have been documented in events elsewhere (Wang and Manga, 2015) and such an effect could potentially enhance landslide runout.

Most mapped landslides had L/H ratios close to 1, with a mean value of 1.17 (Fig. 10A, B). Thus, although Gorkha-induced landslides had relatively low S/F ratios compared to global averages, in terms of L/H they were not exceptionally mobile compared to larger volume, highly mobile landslides (e.g., Dade and Huppert, 1998). Prior studies suggest a size threshold (10^5 to 0.5×10^6 m³) beyond which L/H rises significantly as larger landslide masses travel long distances over relatively shallow slopes (Scheidegger, 1973; Hsu, 1975). Most of the Gorkha-triggered landslides were smaller than this threshold, though we observe a lack of increase in L/H with increasing volume of landslides even for those failures that we estimate were $> 10^6$ m³ (Fig. 10A). This observation is consistent with studies that examine runout characteristics of small volume landslides and is in contrast with the well known "size effect" on L/ H for larger landslide volumes (above $\sim 10^5 \text{ m}^3$), in which case runout distances relative to height drop increase with volume (e.g., Dade and Huppert, 1998; Corominas, 1996).

We isolated landslides with L/H ratios above 2 and runout distances $> 200 \, \mathrm{m}$ (38 landslides) and identify these as highly mobile relative to the rest of the inventory. The number of highly mobile landslides peaks strongly at elevations 2500–3000 m, with more highly mobile landslides above 4000 m than are found in the main distribution (Fig. 10C). The preference for higher elevations in this distribution likely reflects changes in landscape morphology and surface-forming materials at higher elevation and higher relief in this region. For example,

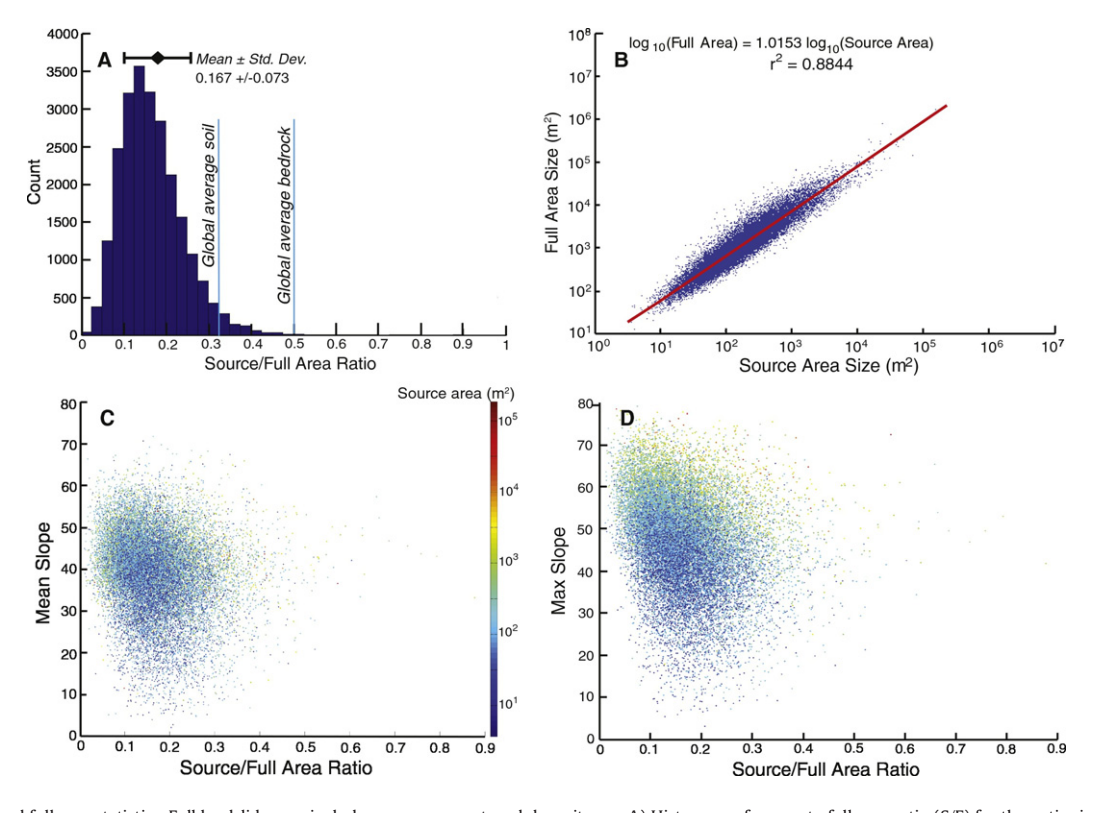


Fig. 9. Source area and full area statistics. Full landslide area includes source, runout, and deposit area. A) Histogram of source to full area ratio (S/F) for the entire inventory. B) Log-log relationship of source to full area. C) Scatter plot of source area size (color) as a function of source to full area ratio and mean slope of full landslide area. D) Scatter plot of source area size (color) as a function of source to full area ratio and maximum slope of full landslide area.

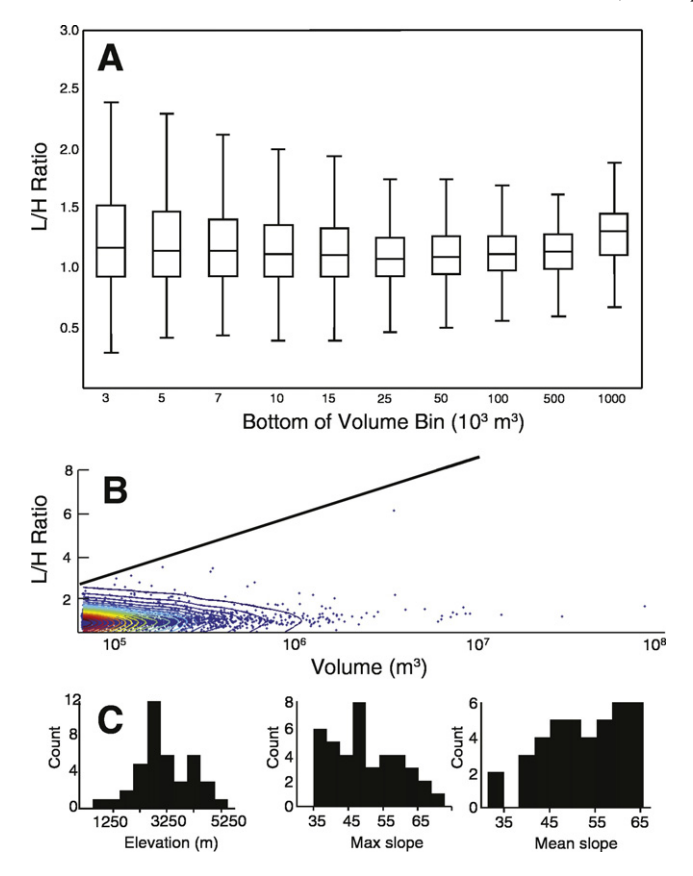


Fig. 10. Length to height mobility index. A) L/H ratio as a function of landslide volume. B) Scatter plot of L/H ratio as a function of volume. Point density is represented with contour intervals where red is high density and blue is low density. Black line represents previously known upper bound behavior for rock and debris avalanches (Iverson et al., 2015; Dade and Huppert, 1998). C) Histograms of highly mobile landslides as a function of elevation, maximum and mean slope of full landslide area.

landslide mobility can be increased by movement across snow or ice-covered surfaces, and by steep slopes (Nicoletti and Sorriso-Valvo, 1991), all of which are more prevalent at higher elevations in the affected region. However, we note that the deadly Langtang landslide (Kargel et al., 2016), which traveled > 3 km, originated from a very high slope (2 km) such that the resulting L/H ratio is not remarkable.

3.6. Connectivity of landslide debris with the river system

The mobility of landslides also influences the potential for landslide debris to be deposited within the fluvial system, where it contributes to erosional budgets by producing transportable sediment (Dadson et al., 2004; Li et al., 2016) and further affects sediment dynamics by altering fluvial grain size distributions (e.g., Attal et al., 2015). Such deposition is referred to as "connectivity", which is a function of the landslide runout path and its intersection with stream channels. The minimum drainage area by which a "channel" is defined affects connectivity because a majority of the cumulative length of the drainage network lies within steep headwater catchments. Defining an appropriate minimum critical drainage area for the initiation of channel heads (Ac) depends on how much transfer of landslide debris occurs from low-order channels, which is likely to be a function of the local catchment characteristics and climatology (e.g. Johnson and Sitar, 1990; Benda and Dunne, 1997; Johnson et al., 2010; Loye et al., 2016). For example, intense monsoon rainfall events in the Himalaya may trigger debris flows in loworder streams and colluvial channels within the Gorkha-affected region and may be expected to promote high hillslope-channel coupling in low order channels.

The regional G-A plot for the area affected by Gorkha-triggered landslides (Fig. 11A) suggests a transition between colluvial and fluvial channels at a drainage area of ~0.48 km² based on steepening of the G-A relationship. This threshold is within the range of areas for fluvial channelization estimated for basins within this region, but at the lower end, with other values of 1 km² reported for the nearby Siwalik Hills of central Nepal (e.g., Lague and Davy, 2003). The initiation of visibly identifiable channels (which may be colluvial) in satellite images is at approximately 0.1–0.2 km², similar to a change in slope of the G-A plot at 0.19 km². We calculated connectivity values for both of these thresholds and illustrate the sensitivity to the choice of threshold value in Fig. 11B, noting that assuming higher area thresholds (e.g., 1-3 km²) will make a relatively small difference to our conclusions (within 10% in volume terms). We report connectivity as the percentage of landslides connected to channels, in terms of landslide number, area, and volume (e.g., number of channel connected landslides/total number of landslides × 100), either for the whole inventory (Fig. 11) or for defined increments of landslide area, or other parameters (Fig. 12).

Based on the raster-based criterion that mapped landslide areas overlap directly with identified channels, we calculate that ~15% of landslides by number intersect the fluvial network (i.e., for $A_c=0.48~\rm km^2$; Fig. 11B). These represent 33% of landslide area and ~50% of the volume of landslide debris, because larger landslides are more likely to reach channels (Fig. 12A) and landslide volume scales non-linearly with area. These connectivity values are similar to those found for landslides triggered by the Wenchuan earthquake using a similar methodology (16% of landslides by number, 30% by area, and 43+9/-7% by volume; Li et al., 2016). A greater proportion of landslides in the Gorkha inventory (20% by number, 43% by area, and 60% by volume) intersect channels for $A_c=0.19~\rm km^2$, i.e., based on the criterion of channels being visibly identifiable.

The coarse resolution of the 30-m DEM and the potential for landslide debris near channels to interact with the river system means that these connectivity values based only on drainage area may not accurately estimate the potential influence of landslides on sediment dynamics. To explore how estimates of connectivity vary for different assumptions, we also calculate connectivity with a vector-based approach, buffering our channel network at different distances. Based on our definition of where visible channels initiate, 36% of landslides (accounting for 57% of the total landslide area) deliver material to within 50 m of a channel (see example Fig. 11C), 70% deposit within 200 m, and >90% of landslides deposit within 400 m of a channel (Fig. 11D). For a higher drainage threshold, e.g., characteristic of the transition to fluvial channels, about a third of the landslides (28% by number) occur within 50 m of a channel, half within 200 m and three quarters within 400 m (Fig. 11D).

3.7. Variation in landslide-river channel connectivity

In order to consider how connectivity varies across the region affected by Gorkha-triggered landslides, we have calculated the percentage of the landslide volume that is connected to river channels within binned intervals of landslide area (Fig. 12A), runout length (Fig. 12B), elevation (Fig. 12C), and relief (Fig. 12D). In parallel with Wenchuan (Li et al., 2016), we find that connectivity across the Gorkha region is closely correlated with landslide area, with larger landslides more likely to extend fully across hillslopes to reach channels (Fig. 12A). For the Gorkha case, we can confirm that this size-effect is related to increases in runout length for larger landslides (e.g., Fig. 12B). Across the Gorkha inventory, higher connectivity at higher elevations and higher relief (Fig. 12C, D) is likely explained by the increasing landslide size at higher elevation (Fig. 7A). Interestingly, connectivity shows little change between 1 and 2.5 km elevation but increases notably for elevations > 2.5 km (Fig. 12C), which coincides approximately with the physiographic transition between the Lesser and Higher Himalaya. The high-elevation, high-relief regions of the Higher Himalaya are characterized by particularly high connectivity.

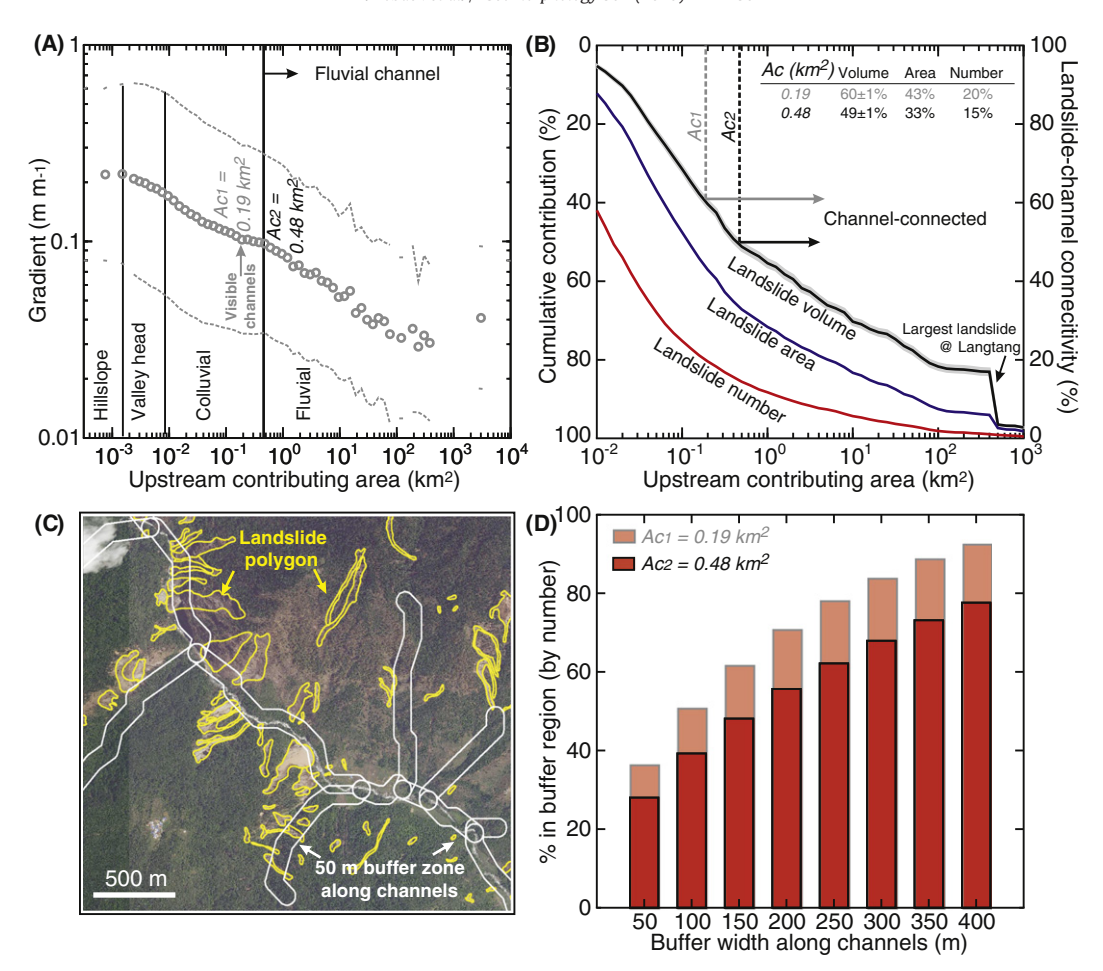


Fig. 11. Connectivity of landslide debris with river systems. A) Gradient-area relationships for the region affected by Gorkha-induced landslides, derived from 30 m resolution SRTM data (open circles: mean hillslope angle in each area bin; dashed lines: ± 1 standard deviation); drainage area thresholds shown for different geomorphic regimes (cf. Montgomery, 2001) and for the area characteristic of the initiation of visible channels in satellite images. B) Proportion of landslide polygons connected with channels as defined by varying drainage area thresholds; values in inset table report % connectivity for the bedrock and alluvial thresholds from (A). C) Sample image showing buffer zones along channels in relation to landslide polygons (example here shows 50 m buffer width). D) Variation in connectivity as a function of buffer width along stream channels.

Mobility indices vary little across the Gorkha inventory and appear to exert only a weak influence on connectivity (Fig. 12E-H shows volumetric connectivity, as in Fig. 12A-D, but plotted for increments of each mobility index). The much larger range in landslide areas (~3 orders of magnitude) may mask any second-order influence of mobility (which varies by at most a factor of 2–3). We have also calculated the median index value (i.e., median S/F or L/H ratio) for each area bin and compare these average index values with connectivity (Fig. 12I-L). Connectivity is highest for the groups of landslides with lowest average S/F ratios and highest L/H ratios (Fig. 12I, J). Both observations reflect the longer travel distance of larger-area landslides. Consistent with our observations about mobility, we find that relief and the maximum slope within landslide areas are positively related to connectivity (Fig. 12K), likely because of their influence on runout length (Fig. 7B), while mean slope has a less clear effect on runout length (Fig. 7C) or connectivity (Fig. 12L). Although these second-order effects are identifiable, mobility overall exerts a less significant control on connectivity in the Gorkha case than might have been expected a priori, largely because of the relatively small variation in mobility across the inventory (Fig. 12E-H).

4. Discussion

4.1. Comparison to other inventories of earthquake-triggered landslides

Initial studies suggested that the number of landslides associated with the Gorkha event (Kargel et al., 2016) was about an order of

magnitude lower than expected based on other landslide-triggering earthquakes (cf. Malamud et al., 2004). However, our comprehensive mapping of the affected area with high-resolution images suggests that the total number (n = 24.915) and area (87 km²) of Gorkha-triggered landslides identified to date (July 2016) is average for the moment magnitude release of this event when compared to prior global compilations (Fig. 13; Malamud et al., 2004; Keefer, 1994). Landslide number and to a lesser extent area can be sensitive to mapping resolution, while volume estimates are likely to be less biased since the overall volume contribution from small-area landslides, which would be overlooked in low-resolution mapping, tends to be small (Stark and Hovius, 2001; Li et al., 2014). Interestingly, our estimate of the total Gorkha landslide volume $(0.81 + 0.11/-0.09 \text{ km}^3 \text{ assuming the Hima-}$ layan scaling parameters from Larsen et al., 2010) also matches well with the first-order trend between earthquake magnitude and landslide volumes for past events (Fig. 13). Marc et al. (2016) presented a mechanistic model describing coseismic landslide volumes and predicted a volume for the Gorkha event $(0.30 + 0.16/-0.11 \text{ km}^3)$ assuming a globally average value for their tuning parameter that describes "material sensitivity" to landsliding; we calculate a similar volume from their model $(0.33 + 0.26/-0.14 \text{ km}^3)$ using updated estimates of source depth (\sim 10 \pm 2 km; Wang and Fialko, 2015; Duputel et al., 2016; Elliott et al., 2016) and modal slope across the region mapped in this study (28 \pm 8°, 1 standard deviation). Material sensitivity is not independently well known, and nor are the most appropriate area-volume scaling parameters, so although these model predictions do not overlap

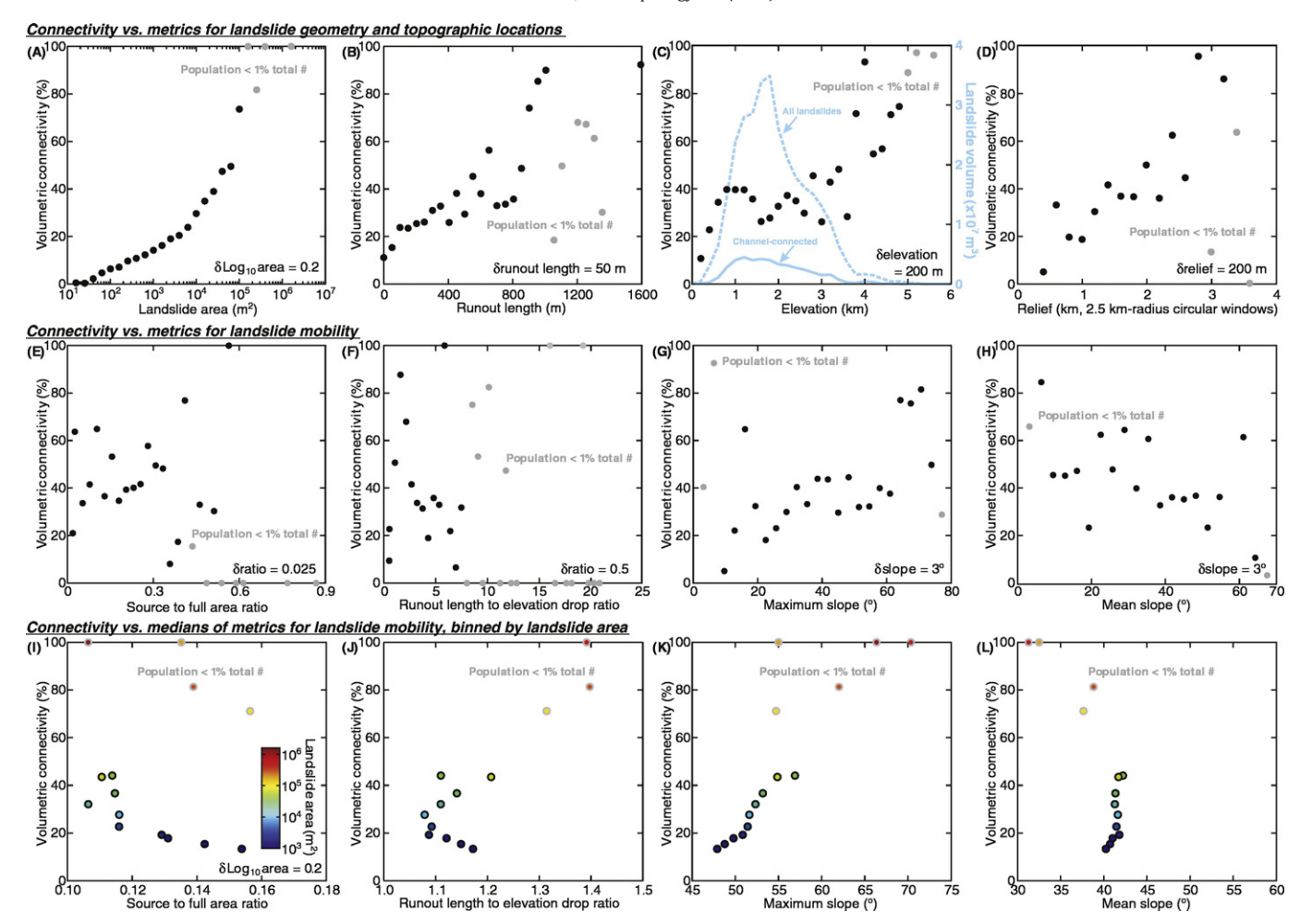


Fig. 12. Correlation between connectivity (% of landslide volume connected to bedrock channels, as defined in the text, within each binning increment) and metrics for landslide geometry, landslide location, and mobility. A)–H) Connectivity calculated for landslide populations binned by: A) landslide area; (B) runout length; (C) elevation; (D) relief, calculated as the range of elevation in 2.5 km-radius circular windows; E) source to full area ratio (S/F); F) runout length to elevation drop ratio (L/H); G) maximum slope in landslide polygons; H) mean slope in landslide polygons. Bin intervals shown on each figure. I)–through L) Landslides are grouped by landslide area as in (A); data points show connectivity and medians values from the landslide population in each area bin of the indexes of mobility as in E)–H). Colors of the points refer to landslide area as shown by the colorbar. We chose 1% of the total landslide number as a threshold to determine statistical significance. If the landslide number in a bin is <1% of the total landslide number, the data point representing the bin is assigned as statistically insignificant (grey color), and vice versa. We have tested other thresholds from 0.5% to 1%, and the relations were consistent.

exactly with our estimates from mapping, the first-order similarity again suggests that the Gorkha event was consistent with other land-slide-triggering earthquakes (Fig. 13). Overall, we thus conclude that the magnitude of the Gorkha-triggered landslide event was average for the earthquake moment magnitude.

The initial impression of less landslide activity than expected (Kargel et al., 2016) may have resulted from incomplete mapping in the immediate aftermath due to the paucity of available imagery, the remoteness of much of the affected region, and a tendency to compare this event to the 2008 M_w7.9 Wenchuan earthquake (cf. Xu et al., 2016), which caused an anomalously large number of landslides relative to its magnitude (e.g., Marc et al., 2016). The Wenchuan earthquake shared similarities with the Gorkha event that make comparison tempting, for example, similar magnitude and similar setting along the margin of the Tibetan Plateau. However, the maximum PGA during the Wenchuan event is thought to have been considerably higher (0.9 g vs. 0.6 g for Gorkha; from USGS ShakeMaps for each event) and the return time longer (500-3000 yrs for Wenchuan vs. <100 yrs for Gorkha; Densmore et al., 2007; Mencin et al., 2016), although it is important to point out that PGA is much less well constrained for Gorkha compared to Wenchuan. Recurrence times may influence co-seismic landsliding by changing slope pre-conditioning (e.g., Parker et al., 2015). The fault geometry was also distinctly different, with a steep reverse fault producing high PGA in the region of highest relief in Wenchuan (Liu-Zeng et al., 2009), compared to the shallow, probably ramped mega-thrust geometry that resulted in spatially complex release of 0.5–2 Hz seismic energy during the Gorkha earthquake (Avouac et al., 2015) and probable separation between the area of highest slopes and the area of highest PGA (see further discussion below). All of these factors could contribute to explaining differences between the Gorkha and Wenchuan landslide events despite similarity in moment magnitude release, topography, climate, and rock type.

4.2. Seismotectonic and climatic influences on landslide density?

A main first-order feature of the Gorkha inventory is the abrupt onset of landsliding north of the physiographic transition. Gallen et al. (2017) showed that this feature could be reproduced from a forward model using uniform rock strength, published PGA model values for the Gorkha event, and 90 m resolution digital topography. Such a prediction takes into account the competing effects of PGA, which is higher for the Lesser Himalaya/Middle Hills, and slope, which increases in the High Himalaya, to suggest that the availability of steep slopes across this transition is responsible for the abrupt increase in landslide density (Figs. 1, 6). Because the maximum PGA and maximum slope are offset by about 50 km, landslide density is highest at the cross-over between elevated PGA and slope (e.g., Fig. 6A, B).

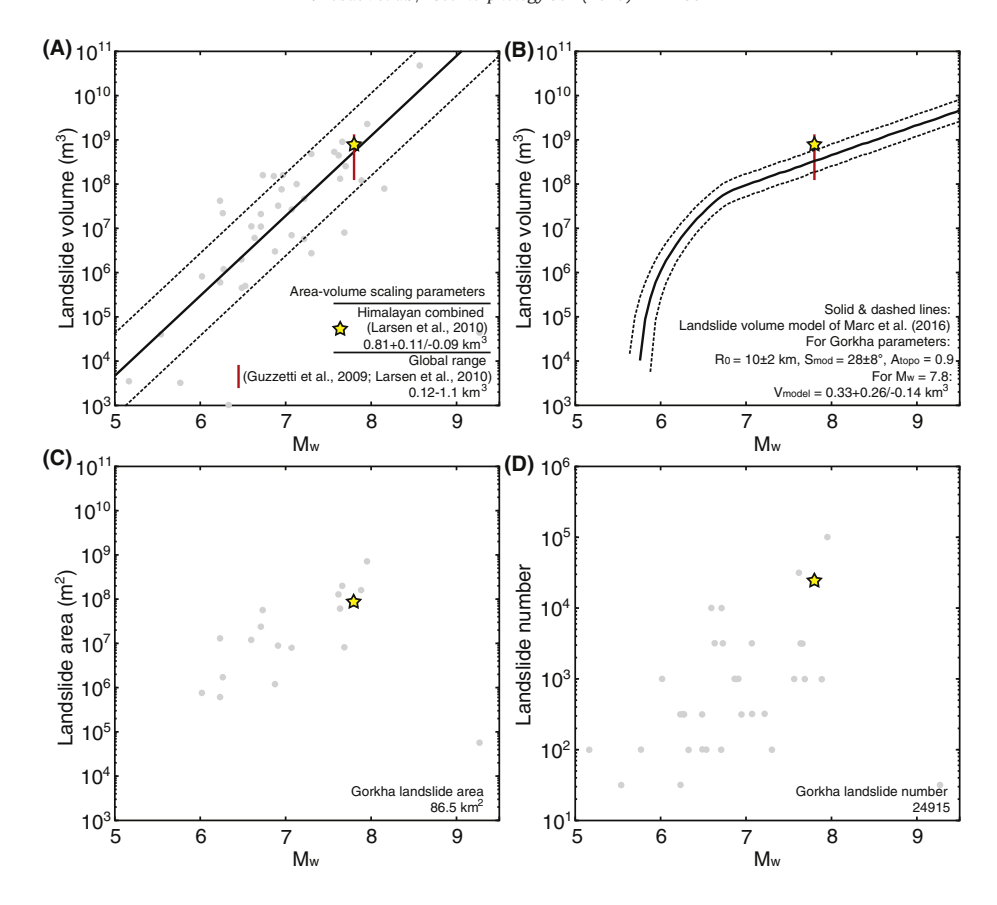


Fig. 13. Gorkha landslide inventory compared to global relationships between total landslide volume, area and number and earthquake moment magnitude. A) Gorkha landslide volume (star) and volumes from other major earthquake events (grey dots; compiled by Marc et al., 2016) vs. earthquake magnitude; solid line: empirical regression of the global data; dashed lines: ±1 sigma residual of least squares fit. B) Gorkha landslide volume (star) in context of predictive model (Marc et al., 2016) using Gorkha parameters as shown on figure; solid curve and dashed lines represent the median and the 68% confidence intervals, respectively. C and D) Gorkha landslide area and number, respectively, as stars, in relation to compilation of data from previous earthquakes, as grey dots (Marc et al., 2016).

Another noteworthy feature of the Gorkha inventory is the much lower landslide density in even steeper slopes within the High Himalaya, Figs. 5 and 6 show that landslide density is highest at mid elevations (2-3 km), moderately high slopes (~60°), and moderately high relief (~2 km). Landslide density decreases markedly at higher elevations (>4 km), higher slopes (>70°) and higher relief (3–4 km), without significant decrease in PGA. In general, we expect higher slope and higher relief to be positively correlated with landslide density (Lu and Godt, 2013). The steep, higher relief areas that experienced less landsliding were both farther from the fault plane (and thus likely subject to lower co-seismic ground acceleration) and may have different near surface strength profiles, both of which might explain lower landslide density. Modeled PGA does decrease slightly for the steepest terrain, but the difference is small (e.g., consider 100 km vs. 125 km along the north-south transect in Fig. 6B, and the large range in landslide density for little change in PGA or slope show in the inset Fig. 6C). With only the weakly constrained PGA information from ShakeMap simulations, it is difficult to distinguish conclusively at this stage between the effects of ground acceleration vs. near surface slope strength in determining the low landsliding on the steepest slopes.

Though mapped lithological unit does not appear to exert an identifiable control on landslide occurrence for this event (Figs. 2, 4), slope strength as a function of weathering may play an important role, including in soil and variably weathered and fractured bedrock (Gallen et al., 2015). For example, lower elevation slopes may be weaker as a result of being more weathered than their higher elevation counterparts, because they are both wetter and more vegetated (Gallen et al., 2017; West et al., 2002). High mean annual precipitation coincides with high landslide density; again comparing between 100 km vs. 125 km along

the S-N profile in Fig. 6, slopes increase and PGA declines only slightly, while both precipitation and landslide density decrease dramatically – and the decrease in landslide density mimics the northward decrease in rainfall. We speculate that higher degrees of chemical and physical weathering in the near surface rock profile may have promoted a greater number of slope failures in regions of highest landslide density, as has been suggested for the 2008 M_w 7.9 Wenchuan Earthquake in China (Gallen et al., 2015).

We also expect some of the scatter in the relationships between PGA, slope, and landslide density to relate to our limited current capacity to accurately characterize the seismic energy responsible for landslides during this event. The deep portion of the slip patch, above which landslides are most concentrated, is thought to have radiated 0.5-2 Hz seismic energy during rupture (Galetzka et al., 2015; Avouac et al., 2015). We suggest that the proximity of this focused, seismic energy release to the steep topography near the physiographic transition may be related to the location of landslides, and speculate that focusing of seismic energy due to eastward propagation of the rupture may also in part explain the west-to-east increase in landslide density (Fig. 6D-F). We anticipate being able to further refine estimates of PGA, rock strength, and topography as post-event studies mature over the coming few years, and these additional data will provide the necessary input for modeling of the combined effect of ground motion, material strength, and slope on seismic slope stability.

Based on paleoseismic records, the Gorkha earthquake was an intermediate sized earthquake for the Himalayan fault system (Bilham et al., 2001; Lavé et al., 2005; Kumar et al., 2010). Therefore, we might expect a more intense landslide event with a surface breaking rupture of magnitude 8 or 9 (i.e., a "great" Himalaya earthquake; Stevens and Avouac,

2016). In particular, we anticipate that the highest risk associated with coseismic landslides may be concentrated near the physiographic transition above the deepest portion of the locked fault plane, if the source characteristics of Gorkha event are typical of larger ruptures. Severe ground shaking associated with a great Himalaya event may also trigger more deeply seated landslides with greater volume and mobility, and an increased number of valley-blocking landslide dams on the transverse Himalaya river systems.

4.3. Controls on landslide mobility during the Gorkha earthquake

In principle, the forces that initiate and sustain movement of the landslide mass, as well as the frictional characteristics of the mass and sliding plane, dictate mobility. Though these factors can all vary, compilations of landslide statistics over a range of size and environments show coherent trends. The Gorkha-induced landslides generally have small source areas and long, narrow runout paths. The observed L/H ratio ~1 (i.e., ~45°) agrees closely with the mean topographic slope (~ 40°). This indicates not only that landslides developed in steep topography, but also that runout areas of landslides generally were confined to areas of steep topography, with little runout over shallowly dipping surfaces or along stream channels. Many landslides that developed on steep slopes in Greater Himalayan river gorges extend to river channels or nearby river terraces at the bottom of steep valleys (Fig. 11). The lack of shallow slopes in areas densely affected by landsliding and the abrupt termination of landslides at valley bottoms generally limit L/H ratios to values ~1, regardless of the size of landslide considered (Fig. 10). We thus propose that the extreme topography in Nepal likely controlled the L/H ratio. The observation of little runout over other more shallowly sloped areas such as agricultural terraces may also reflect the small source areas and material volumes, such that these were not energetic enough to travel long distances over shallowly sloped terrain and lacked the sustained development of positive pore-water pressures in the moving mass that enhances landslide mobility (Iverson, 1997). We expect that the dry conditions at the time of the Gorkha earthquake (Collins and Jibson, 2015) minimized the hydrological enhancement of landslide mobility. Overall, our observations are consistent with similar L/H values (close to 1) obtained from a study of 3000 shallow, small landslides in Hong Kong (Finlay et al., 1999).

4.4. Connectivity and its potential influence on sediment dynamics

Our analysis suggests that roughly half or more of the total landslide volume was directly connected to channels. Connectivity is highest for landslides at higher elevations, where slopes are steepest, relief is greatest, and average landslide areas are largest (Figs. 7, 12). Although there is less total volume of landslide debris at high elevations (2500-4000 m) compared to mid-elevations (1000-2500 m), as shown in Fig. 12C, the landslides that are present at high elevations are more likely to directly impact sediment dynamics. Thus consideration of the potential for future sediment-related cascading hazards such as channel aggradation and increased flooding risk should not focus solely on the regions of highest landslide density. At the same time, our analysis suggests that, particularly at mid-elevations (1–2 km), just over half of the volume of landslide debris was deposited on hillslopes or in steep, colluvial channels, not connected with channels with drainage area >0.4 km². Potentially, intense precipitation events associated with the monsoon season may remobilize unconsolidated material in colluvial channels to form debris flows (cf. Prancevic and Lamb, 2015) with damaging consequences. On the other hand, landslide material away from ephemeral colluvial channels may be in a more stable position after the earthquake (i.e. at a lower slope angle and greater factor of safety) than it was prior to the earthquake. The tradeoff between the topographic position of this material and its lower cohesion as compared to before the earthquake is likely to determine its susceptibility to be transported in later storm events. The net effect of coseismic landslide debris on future debris flow hazard warrants further study and should include a more detailed investigation of where landslide material resides for drainage areas $<\!0.4~\rm km^2$, particularly with reference to local precipitation patterns.

Though connectivity indicates the potential for landslide debris to interact with the fluvial system directly, the conditions that determine actual sediment transport are complex and likely to depend not only on connectivity as calculated here, but also on grain size, channel geometry, and discharge, amongst other parameters (e.g., Lamb et al., 2008). Many of the channel intersections we have identified are in higher order tributaries with drainage area of $10^5 - 10^6$ m², which may influence the potential for fluvial sediment transport because discharge may be small or ephemeral. In other cases, larger landslides may deliver material that is readily mobilized from the distal portion of the deposit, while material in the same deposit, but farther from the river channel, may not be so easily transported. For some of the landslides that did not reach the stream channel during the coseismic period, we observed in the field and in satellite imagery that later monsoon rain events produced debris flows that connected the coseismic landslide with rivers and thus transported coseismic landslide material to the fluvial network. We have not undertaken a systematic study of post-monsoon changes to quantify this effect, but it may play an important role in determining the effect of this event on sediment dynamics in the Himalaya.

5. Conclusions

The 25 April 2015, M_w7.8 Gorkha earthquake triggered at least ~ 25,000 landslides mapped in this study. These landslides comprise a number, area, and volume that are consistent with the moment magnitude of this event based on data from past landslide-triggering earthquakes (e.g., Malamud et al., 2004; Marc et al., 2016), in contrast to early reports from hazard-based assessments (Kargel et al., 2016). The density of landslides (defined by number of landslides per unit area) showed no preference for lithologic units, with the densest landsliding mostly observed at lower elevations in Greater Himalayan river gorges, despite steeper slopes at higher altitudes. In this event, the area of steepest slopes is offset by about 50 km from the region of highest modeled PGA. We observe focusing of landslide activity between these two regions of high PGA and steepest slope, where the contribution of each factor is likely maximized. We speculate that seismic energy emitted from the deepest part of the rupture patch may have played a role in focusing landslide activity along the frontal High Himalaya and in the direction of rupture propagation. Together with the shallower slopes to the south, this pattern may explain the decoupling between modeled PGA and landslide density. The coincidence of the highest density landsliding with high precipitation also suggests a potential climatic role in determining rock strength, perhaps by weakening the shallow subsurface by weathering (e.g., Gallen et al., 2015) especially compared to the drier, high elevation alpine landscapes.

The values of landslide mobility indices obtained for this inventory mainly reflect the influence of steep topography and high relief of the Himalayan mountain range. High source to full landslide area ratios reflect the ability of landslide material from small sources to travel long distances, but only over long, steep hillslopes; little to no runout across shallower slopes was observed, and a high percentage of landslides terminate at or within 200 m of valley bottoms. Thus valley topography appears to limit downslope transport, and most landslides intersect channels within a few hundred meters. This phenomenon results in a high potential for the connectivity of landslide debris with the fluvial network, which suggests that earthquakes are coupled to the longterm sediment budget and geochemical cycling in the Himalaya. In particular, the generally larger area of landslides at higher elevations means that these failures are more prone to connect directly to fluvial channels compared to their counterparts at lower elevations, suggesting that they may exert a disproportionate effect on sediment dynamics relative

to their total mapped area. In contrast, the high proportion of landslide deposits remaining outside of the fluvial domain, particularly at mid-elevations, may enhance the risk of debris flows during monsoon rainstorms. The data presented here will provide key input to tracking sediment and chemical fluxes as coseismic landslides are reactivated and enlarged in coming monsoon seasons.

Acknowledgments

This work was supported by a National Science Foundation (NSF) RAPID award from the Geomorphology and Land Use Dynamics program (EAR-1546630) to West and EAR-1546631 to Clark and a collaborative research award to West (EAR-1640894) and Clark/Zekkos (EAR-1640797), with partial support from University of Michigan internal award to Clark and Zekkos (MCubed 2.0 Project ID 917). Gallen received support from a Swiss Federal Institute of Technology (ETH) Research Commission grant no. ETH-15 15-2. We thank Paul Morin from the PGC (Polar Geospatial Center) for providing imagery access and support for acquiring satellite data through a NGA (National Geospatial-Intelligence Agency) cooperative agreement with NSF. We also thank William Greenwood, Julie Bateman, Bibek Giri, Kristen Cook, Maarten Lupker and John Galetzka for their assistance during a 2015 field expedition to Nepal, and Jean-Philippe Avouac, Bodo Bookhagen, Alex Densmore, Odin Marc and Diego Melgar for helpful discussions. Issac Larsen, Kate Allstadt and one anonymous reviewer provided feedback that improved the manuscript. Any use of trade, firm, or product names is for descriptive purposes only and does not imply endorsement by the U.S. Government.

References

- Ader, T., Avouac, J.P., Liu-Zeng, J., Lyon-Caen, H., Bollinger, L., Galetzka, J., Genrich, J., Thomas, M., Chanard, K., Nath Sapkota, S., Rajaure, S., Shrestha, P., Ding, L., Flouzat, M., 2012. Convergence rate across the Nepal Himalaya and interseismic coupling on the Main Himalayan Thrust: implications for seismic hazard. J. Geophys. Res. Solid Earth 117 (B4). http://dx.doi.org/10.1029/2011JB009071.
- Andermann, C., Bonnet, S., Gloaguen, R., 2011. Evaluation of precipitation data sets along the Himalayan front. Geochem. Geophys. Geosyst. 12 (7). http://dx.doi.org/10.1029/2011.0003513
- Attal, M., Mudd, S.M., Hurst, M.D., Weinman, B., Yoo, K., Naylor, M., 2015. Impact of change in erosion rate and landscape steepness on hillslope and fluvial sediments grain size in the Feather River basin (Sierra Nevada, California). Earth Surf. Dyn. 3 (1):201–222. http://dx.doi.org/10.5194/esurf-3-201-2015.
- Avouac, J.P., Meng, L., Wei, S., Wang, T., Ampuero, J.P., 2015. Lower edge of main Himalayan Thrust unzipped by the 2015 Gorkha earthquake. Nat. Geosci. 8:708–711. http:// dx.doi.org/10.1038/NGEO2518.
- Benda, L., Dunne, T., 1997. Stochastic forcing of sediment supply to channel networks from landsliding and debris flow. Water Resour. Res. 33 (12), 2849–2863.
- Bilham, R., 2004. Earthquakes in India and the Himalaya: tectonics, geodesy, and history. Ann. Geophys. 47, 839–858.
- Bilham, R., Gaur, V.K., Molnar, P., 2001. Himalayan seismic hazard. Science 293: 1442–1444. http://dx.doi.org/10.1126/science.1062584.
- Bollinger, L., Sapkota, S.N., Tapponier, P., Klinger, Y., Rizza, M., Van der Woerd, J., Tiwari, D.R., Pandey, R., Bitri, A., Bes de Berc, S., 2014. Estimating the return times of great Himalayan earthquakes in eastern Nepal: evidence from the Patu and Bardibas strands of the Main Frontal Thrust. J. Geophys. Res. Solid Earth. http://dx.doi.org/10.1002/2014JB010970.
- Bookhagen, B., Burbank, D.W., 2010. Toward a complete Himalayan hydrological budget: Spatiotemporal distribution of snowmelt and rainfall and their impact on river discharge. J. Geophys. Res. Earth Surf. 115 (F3). http://dx.doi.org/10.1029/2009JF001426.
- British Geological Survey (BGS), 2015. Preliminary Landslide Inventory Following 25 April 2015 Nepal Earthquake. (Accessed at: http://www.bgs.ac.uk/research/earthHazards/epom/documents/LandslideinventoryNepal8 May2015.pdf).
- Collins, B.D., Jibson, R.W., 2015. Assessment of Existing and Potential Landslide Hazards Resulting from the April 25, 2015 Gorkha, Nepal Earthquake Sequence, USGS Open-File Report 2015-1142. http://dx.doi.org/10.3133/ofr20151142.
- Corominas, J., 1996. The angle of reach as a mobility index for small and large landslides. Can. Geotech. J. 33, 260–271.
- Craddock, W.H., Burbank, D.W., Bookhagen, B., Gabet, E.J., 2007. Bedrock channel geometry along an orographic rainfall gradient in the upper Marsyandi River valley in central Nepal. J. Geophys. Res. 112, F03007. http://dx.doi.org/10.1029/2006JF000589.
- Crosta, G.B., Hermanns, R., Frattini, P., Valbuzzi, E., Valagussa, A., 2014. Large slope instabilities in Northern Chile: inventory, characterization and possible triggers. Landslide Science for a Safer Geoenvironment. Springer International Publishing, pp. 175–181. Dade, W.B., Huppert, H.E., 1998. Long-runout rockfalls. Geology 26 (9), 803–806.

- Dadson, S.J., Hovius, N., Chen, H., Dade, W.B., Lin, J.C., Hsu, M.L., Lin, C.W., Horng, M.J., Chen, T.C., Milliman, J., Stark, C.P., 2004. Earthquake-triggered increase in sediment delivery from an active mountain belt. Geology 32 (8), 733–736.
- Dai, F.C., Xu, C., Yao, X., Tu, X.B., Gong, Q.M., 2011. Spatial distribution of landslides triggered by the 2008 Ms 8.0 Wenchuan earthquake, China. J. Asia Earth Sci. 40: 883–895. http://dx.doi.org/10.1016/j.jseaes.2010.04.010.
- Davies, T.R.H., 1982. Spreading of rock avalanche debris by mechanical fluidization. Rock Mech. 15, 9–24.
- Densmore, A.L., Ellis, M.A., Li, Y., Zhou, R., Hancock, G.S., Richardson, N., 2007. Active tectonics of the Beichuan and Pengguan faults at the eastern margin of the Tibetan Plateau. Tectonics:26. http://dx.doi.org/10.1029/2006TC001987.
- Dhital, M.R., 2015. Geology of the Nepal Himalaya: Regional Perspective of the Classic Collided Orogen. Springer International Publishing, Switzerland. http://dx.doi.org/10. 1007/978-3-319-02496-7.
- Duputel, Z., Vergne, J., Rivera, L., Wittlinger, G., Farra, V., Hetenyi, G., 2016. The 2015 Gorkha earthquake: a large event illuminating the Main Himalayan Thrust fault. Geophys. Res. Lett. 43. 2517–2525.
- Earle, P.S., Wald, D.J., Jaiswal, K.S., Allen, T.I., Marano, K.D., Hotovec, A.J., Hearne, M.G., Fee, J.M., 2009. Prompt Assessment of Global Earthquakes for Response (PAGER): a system for rapidly determining the impact of global earthquakes worldwide. In: Survey, U.S.G.S. (Ed.), Open-File Report 2009-1131.
- Earthquakes Without Frontiers (EWF), 2015. UPDATED (30 June) Landslide Inventory Following 25 April and 12 May Earthquakes: Earthquakes Without Frontiers Blog. http://ewf.nerc.ac.uk/2015/06/30/updated-30-june-landslide-inventory-following-25-april-and-12-may-nepal-earthquakes/.
- Elliott, J.R., Jolivet, R., González, P.J., Avouac, J.P., Hollingsworth, J., Searle, M.P., Stevens, V.L., 2016. Geometry of the Main Himalayan Thrust fault and relation to topography revealed by the Gorkha earthquake. Nat. Geosci. 9:174–180. http://dx.doi.org/10. 1038/ngeo2623.
- Farr, T.G., et al., 2007. The shuttle radar topography mission. Rev. Geophys. 45 (2). http://dx.doi.org/10.1029/2005RG000183.
- Finlay, P.J., Mostyn, G.R., Fell, R., 1999. Landslide risk assessment: prediction of travel distance. Can. Geotech. J. 36 (p), 556–562.
- Gabet, E.J., Pratt-Sitaula, B.A., Burbank, D.W., 2004. Climactic controls on hillslope angle and relief in the Himalayas. Geology 32 (7):629–632. http://dx.doi.org/10.1130/ G20641.1.
- Galetzka, J., Melgar, D., Genrich, J.F., Geng, J., Owen, S., Lindsey, E.O., Xu, X., Bock, Y., Avouac, J.P., Adhikari, L.B., Upreti, B.N., 2015. Slip pulse and resonance of the Kathmandu basin during the 2015 Gorkha earthquake, Nepal. Science 349:1091–1095. http://dx.doi.org/10.1126/science.aac6383.
- Gallen, S.F., Clark, M.K., Godt, J.W., 2015. Coseismic landslides reveal near-surface rock strength in a high-relief, tectonically active setting. Geology 43:11–14. http://dx.doi. org/10.1130/G36080.1.
- Gallen, S.F., Clark, M.K., Godt, J.W., Roback, K., Niemi, N.A., 2017. Application of a Rapid Response Earthquake-Triggered Landslide Model to the 25 April 2015 Mw, 7.8 Gorkha earthquake, Nepal. Tectonophysics. http://dx.doi.org/10.1016/j.tecto.2016.10.031.
- Gerrard, J., Gardner, R.A.M., 2000. Relationships between rainfall and landsliding in the Middle Hills, Nepal. Nor. J. Geol. 54:74–81. http://dx.doi.org/10.1080/002919500423807.
- Guo, D., Hamada, M., He, C., Wang, Y., Zou, Y., 2014. An empirical model for landslide travel distance prediction in Wenchuan earthquake area. Landslides 11, 281–291.
- Guzzetti, F., Ardizzone, F., Cardinali, M., Rossi, M., Valigi, D., 2009. Landslide volumes and landslides mobilization rates in Umbria, central Italy. Earth Planet. Sci. Lett. 279: 222–229. http://dx.doi.org/10.1016/j.epsl.2009.01.005.
- Hayes, G.P., Briggs, R.W., Barnhart, W.D., Yeck, W.L., McNamara, D.E., Wald, D.J., Nealy, J.N., Benz, H.M., Gold, R.D., Jaiswal, K.S., Marano, K., Earle, P.S., Hearne, M.G., Smoczyk, G.M., Wald, L.A., Samsonov, S.V., 2015. Rapid characterization of the 2015 M_w 7.8 Gorkha, Nepal, earthquake sequence and its seismotectonic context. Seismol. Res. Lett. 86:1557–1567. http://dx.doi.org/10.1785/0220150145.
- Heim, A., 1932. Trans. by Skermer, N. Landslides & Human Lives: BiTech, British Columbia (195 pp., ISBN: 9780921095064).
- Hovius, N., Stark, C.P., Allen, P.A., 1997. Sediment flux from a mountain belt derived by landslide mapping. Geology 25:231–234. http://dx.doi.org/10.1130/0091-7613(1997)025<0231:SFFAMB>2.3.CO;2.
- Hovius, N., Meunier, P., Lin, C.-W., Chen, H., Chen, Y.-G., Dadson, S., Horng, M.-J., Lines, M., 2011. Prolonged seismically induced erosion and the mass balance of a large earthquake. Earth Planet. Sci. Lett. 304:347–355. http://dx.doi.org/10.1016/j.epsl.2011.02. 005
- Hsu, K., 1975. Catastrophic debris streams (Sturzstroms) generated by rockfalls. Geol. Soc. Am. Bull. 86, 129–140.
- Huang, R., Fan, X., 2013. The landslide story. Nat. Geosci. 6:325–326. http://dx.doi.org/10. 1038/ngeo1806.
- Huang, A.Y.L., Montgomery, D.R., 2014. Topographic locations and size of earthquake- and typhoon-generated landslides, Tachia River, Taiwan. Earth Surf. Process. Landf. 39 (3):414–418. http://dx.doi.org/10.1002/esp.3510.
- Hunter, G., Fell, R., 2003. Travel distance angle for "rapid" landslides in constructed and natural soil slopes. Can. Geotech. J. 40, 1123–1141.
- ICIMOD, 2015. Landslides and Damage Maps, Nepal Earthquake. 2015 Accessed at:. http://www.icimod.org/?q=17904.
- Iverson, R.M., 1997. The physics of debris flows. Rev. Geophys. 35 (3), 245-296.
- Iverson, R.M., George, D.L., Allstadt, K., Reid, M.E., Collins, B.D., Vallance, J.W., Schilling, S.P., Godt, J.W., Cannon, C.M., Magirl, C.S., Baum, R.L., 2015. Landslide mobility and hazards: implications of the 2014 Oso disaster. Earth Planet. Sci. Lett. 412:197–208. http://dx.doi.org/10.1016/j.epsl.2014.12.020.
- Jin, Z., West, A.J., Zhang, F., An, Z., Hilton, R.G., Yu, J., Wang, J., Li, G., Deng, L., Wang, X., 2015. Seismically enhanced solute fluxes in the Yangtze River headwaters following

- the A.D. 2008 Wenchuan earthquake. Geology 44:47–50. http://dx.doi.org/10.1130/G37246.1.
- Johnson, K.A., Sitar, N., 1990. Hydrologic conditions leading to debris-flow initiation. Can. Geotech. J. 27 (6), 789–801.
- Johnson, R.M., Warburton, J., Mills, A.J., Winter, C., 2010. Evaluating the significance of event and post-event sediment dynamics in a first order tributary using multiple sediment budgets. Geogr. Ann. Ser. A Phys. Geogr. 92:189–209. http://dx.doi.org/10. 1111/j.1468-0459.2010.00389.x.
- Kargel, J.S., et al., 2016. Geomorphic and geologic controls of geohazards induced by Nepal's 2015 Gorkha earthquake. Science 351 (6269). http://dx.doi.org/10.1126/ science.aac8353.
- Keefer, D.K., 1994. The importance of earthquake-induced landslides to long-term slope erosion and slope-failure hazards in seismically active regions. Geomorphology 10, 265–284
- Keefer, D.K., 2002. Investigating landslide caused by earthquakes a historical review. Surv. Geophys. 23, 473–510.
- Kent, P.E., 1966. The transport mechanism in catastrophic rock falls. J. Geol. 74, 79–83.
- Korup, O., Montgomery, D.R., Hewitt, K., 2010. Glacier and landslide feedbacks to topographic relief in the Himalayan syntaxes. Proceedings of the National Academy of Sciences of the United States of America 107:pp. 5317–5322. http://dx.doi.org/10.1073/pnas.0907531107.
- Kumar, S., Wesnousky, S.G., Jayangondaperumal, R., Nakata, T., Kumahara, Y., Singh, V., 2010. Paleoseismological evidence of surface faulting along the northeastern Himalayan front, India: Timing, size, and spatial extent of great earthquakes. J. Geophys. Res. Solid Earth 115 (B12). http://dx.doi.org/10.1029/2009JB006789.
- Lacroix, P., 2016. Landslides triggered by the Gorkha earthquake in the Langtang valley, volumes and initiation processes. Earth Planets Space 68:46. http://dx.doi.org/10. 1186/s40623-016-0423-3
- Lague, D., Davy, P., 2003. Constraints on the long-term colluvial erosion law by analyzing slope-area relationships at various tectonic uplift rates in the Siwaliks Hills (Nepal). J. Geophys. Res. 108:2129. http://dx.doi.org/10.1029/2002JB001893 B2.
- Lamb, M.P., Dietrich, W.E., Venditti, J.G., 2008. Is the critical Shields stress for incipient sediment motion dependent on channel-bed slope? J. Geophys. Res. Earth Surf. 113, F02008. http://dx.doi.org/10.1029/2007JF000831.
- Larsen, I.J., Montgomery, D.R., Korup, O., 2010. Landslide erosion controlled by hillslope material. Nat. Geosci. 3:247–251. http://dx.doi.org/10.1038/ngeo776.
- Lavé, J., Avouac, J.P., 2000. Active folding of fluvial terraces across the Siwaliks Hills, Himalayas of central Nepal. J. Geophys. Res. Solid Earth 105:5735–5770. http://dx. doi.org/10.1029/1999JB00292.
- Lavé, J., Avouac, J.P., 2001. Fluvial incision and tectonic uplift across the Himalayas of central Nepal. J. Geophys. Res. Solid Earth 106, 26561–26591.
- Lavé, J., Yule, D., Sapkota, S., Basant, K., Madden, C., Attal, M., Pandey, R., 2005. Evidence for a great medieval earthquake (~1100 A.D.) in the central Himalayas, Nepal. Science 307:1302–1305. http://dx.doi.org/10.1126/science.1104804.
- Legros, F., 2002. The mobility of long-runout landslides. Eng. Geol. 63:301–331. http://dx.doi.org/10.1016/S0013-7952(01)00090-4.
- Li, G., West, A.J., Densmore, A.L., Jin, Z., Parker, R.N., Hilton, R.G., 2014. Seismic mountain building: landslides associated with the 2008 Wenchuan earthquake in the context of a generalized model for earthquake volume balance. Geochem. Geophys. Geosyst. 15:833–844. http://dx.doi.org/10.1002/2013GC005067.
- Li, G., West, A.J., Densmore, A.L., Hammond, D.E., Jin, Z., Zhang, F., Wang, J., Hilton, R.G., 2016. Connectivity of earthquake-triggered landslides with the fluvial network: implications for landslide sediment transport after the 2008 Wenchuan earthquake. J. Geophys. Res. Earth Surf.:121 http://dx.doi.org/10.1002/2015JF003718.
- Liu-Zeng, J., Zhang, Z., Wen, L., Tapponnier, P., Sun, J., Xing, X., Hu, G., Zeng, L., Ding, L., Ji, C., Hudnut, K.W., van der Woerd, J., 2009. Co-seismic rupture of the 12 May 2008, M_s 8.0 Wenchuan earthquake, Sichuan: east-west crustal shortening on oblique, parallel thrusts along the eastern edge of Tibet. J. Geophys. Res. Earth Surf. 286:355–370. http://dx.doi.org/10.1016/j.epsl.2009.07.017.
- Loye, A., Jaboyedoff, M., Theule, J.I., Liébault, F., 2016. Headwater sediment dynamics in a debris flow catchment constrained by high-resolution topographic surveys. Earth Surf. Dyn. 4 (2):489–513. http://dx.doi.org/10.5194/esurf-4-489-2016.
- Lu, N., Godt, J.W., 2013. Hillslope Hydrology and Stability. Cambridge University Press. Malamud, B.D., Turcotte, D.L., Guzzetti, F., Reichenbach, P., 2004. Landslides, earthquakes,
- Malamud, B.D., Turcotte, D.L., Guzzetti, F., Reichenbach, P., 2004. Landslides, earthquakes, and erosion. Earth Planet. Sci. Lett. 229:45–59. http://dx.doi.org/10.1016/j.epsl.2004. 10.018.
- Marano, K.D., Wald, D.J., Allen, T.I., 2010. Global earthquake casualties due to secondary effects: a quantitative analysis for improving rapid loss analyses. Nat. Hazards 52 (2):319–328. http://dx.doi.org/10.1007/s11069-009-9372-5.
- Marc, O., Hovius, N., 2015. Amalgamation in landslide maps: effects and automatic detection. Nat. Hazards Earth Syst. Sci. 15:723–733. http://dx.doi.org/10.5194/nhess-15-723-2015.
- Marc, O., Hovius, N., Meunier, P., Gorum, T., Uchida, T., 2016. A seismologically consistent expression for the total area and volume of earthquake-triggered landsliding. J. Geophys. Res. Earth Surf. 121 (4):640–663. http://dx.doi.org/10.1002/2015JF003732.
- Martha, T.R., Roy, P., Mazumdar, R., Govindharaj, K.B., Kumar, K.V., 2016. Spatial characteristics of landslides triggered by the 2015 Mw 7.8 (Gorkha) and Mw 7.3 (Dolakha) earthquakes in Nepal. Landslides: 1–8. http://dx.doi.org/10.1007/s10346-016-0763-x.
- Mathur, L.P., 1953. The Assam earthquake of 15th august, 1950: a short note on factual observations. In: Rao, M.B.R. (Ed.), A Compilation of Papers on the Assam Earthquake of August. 15, 1950, pp. 56–60.
- Mencin, D., Bendick, R., Nath Upreti, B., Pani Adhikari, D., Prasad Gajurel, A., Raj Bhattarai, R., Ram Shrestha, H., Nidhi Bhattari, T., Manandhar, N., Galetzka, J., Knappe, E., Pratt-Sitaula, B., Aoudia, A., Bilham, R., 2016. Himalayan strain reservoir inferred from limited afterslip following the Gorkha earthquake. Nat. Geosci. 9:533–537. http://dx.doi.org/10.1038/ngeo2734.

- Meunier, P., Hovius, N., Haines, A.J., 2007. Regional patterns of earthquake-triggered landslides and their relation to ground motion. Geophys. Res. Lett. 34 (20). http://dx.doi. org/10.1029/2007GL031337.
- Molnar, P., Deng, Q., 1984. Faulting associated with large earthquakes and the average rate of deformation in central and eastern Asia. J. Geophys. Res. Solid Earth 89 (B7), 6203–6227.
- Montgomery, D.R., 2001. Slope distributions, threshold hillslopes, and steady-state topography. Am. J. Sci. 301:432–454. http://dx.doi.org/10.2475/ajs.301.4-5.432.
- Montgomery, D.R., Buffington, J.M., 1997. Channel-reach morphology in drainage basins. GSA Bull. 109:596–611. http://dx.doi.org/10.1130/0016-7606(1997)109<0596: CRMIMD>2.3 CO: 2.
- Montgomery, D.R., Foufoula-Georgiou, E., 1993. Channel network source representation using digital elevation models. Water Resour. Res. 29, 3925–3934.
- Nicoletti, P.G., Sorriso-Valvo, M., 1991. Geomorphic controls of the shape and mobility of rock avalanches. Geol. Soc. Am. Bull. 103, 1365–1373.
- Owen, L.A., Kamp, U., Khattak, G.A., Harp, E.L., Keefer, D.K., Bauer, M.A., 2008. Landslides triggered by the 8 October 2005 Kashmir earthquake. Geomorphology 94:1–9. http://dx.doi.org/10.1016/j.geomorph.2007.04.007.
- Pandey, M.R., Molnar, P., 1988. The distribution of intensity of the Bihar-Nepal earthquake of 15 January 1934 and bounds on the extent of the rupture zone. J. Nepal Geol. Soc. 5 (1), 22–44.
- Parker, R.N., Densmore, A.L., Rosser, N.J., de Michele, M., Li, Y., Huang, R., Whadcoat, S., Petley, D.N., 2011. Mass wasting triggered by the 2008 Wenchuan earthquake is greater than orogenic growth. Nat. Geosci. 4:449–452. http://dx.doi.org/10.1038/ NGE01154.
- Parker, R.N., Hancox, G.T., Petley, D.N., Massey, C.I., Densmore, A.L., Rosser, N.J., 2015. Spatial distributions of earthquake-induced landslides and hillslope preconditioning in the northwest South Island, New Zealand. Earth Surf. Dyn. 3:501–525. http://dx.doi.org/10.5194/esurf-3-501-2015.
- Petley, D., 2012. Global patterns of loss of life from landslides. Geology 40 (10):927–930. http://dx.doi.org/10.1130/G33217.1.
- Petley, D.N., Hearn, G.J., Hart, A., Rosser, N.J., Dunning, S.A., Oven, K., Mitchell, W.A., 2007. Trends in landslide occurrence in Nepal. Nat. Hazards 43 (1):23–44. http://dx.doi.org/ 10.1007/s11069-006-9100-3.
- Prancevic, J.P., Lamb, M.P., 2015. Unraveling bed slope from relative roughness in initial sediment motion. J. Geophys. Res. Earth Surf. 120:474–489. http://dx.doi.org/10. 1002/2014JF003323.
- Qi, S., Xu, Q., Zhang, B., Zhou, Y., Lan, H., Li, L., 2011. Source characteristics of long runout rock avalanches triggered by the 2008 Wenchuan earthquake, China. J. Asia Earth Sci. 40 (4):896–906. http://dx.doi.org/10.1016/j.jseaes.2010.05.010.
- Roback, K., Clark, M.K., West, A.J., Zekkos, D., Gallen, S.F., Chamlagain, D., Godt, J.W., 2017. Map data of landslides triggered by the 25 April 2015 Mw 7.8 Gorkha, Nepal earth-quake. http://dx.doi.org/10.5066/F7DZ06F9.
- Scheidegger, A., 1973. On the prediction of the reach and velocity of catastrophic landslides. Rock Mech. 5, 231–236.
- Schwanghart, W., Bernhardt, A., Stolle, A., Hoelzmann, P., Adhikari, B.R., Andermann, C., Tofelde, S., Merchel, S., Rugel, G., Fort, M., Korup, O., 2016. Repeated catastrophic valley infill following medieval earthquakes in the Nepal Himalaya. Science 351 (6269): 147–150. http://dx.doi.org/10.1126/science.aac9865.
- Sella, G.F., Dixon, T.H., Mao, A., 2002. REVEL: a model for recent plate velocities from space geodesy. J. Geophys. Res. Solid Earth 107. http://dx.doi.org/10.1029/2000JB000033 (ETG 11-1-ETG 11-30).
- Shreve, R.L., 1966. Sherman landslide, Alaska. Science 154, 1639–1643.
- Sklar, L., Dietrich, W.E., 1998. River longitudinal profiles and bedrock incision models: stream power and the influence of sediment supply. In: Tinkler, K.J., Wohl, E.E. (Eds.), Rivers over Rock: Fluvial Processes in Bedrock Channels, American Geophysical Union, Geophysical Monograph 107. Washington, D. C http://dx.doi.org/10.1029/ GM107p0237
- Stark, C.P., Hovius, N., 2001. The characterization of landslide size distributions. Geophys. Res. Lett. 28:1091–1094. http://dx.doi.org/10.1029/2000GL008527.
- Stevens, V.L., Avouac, J.-P., 2016. Millenary Mw > 9.0 earthquakes required by geodetic strain in the Himalaya. Geophys. Res. Lett. 43:1118–1123. http://dx.doi.org/10. 1002/2015GL067336.
- Stock, J., Dietrich, W.E., 2003. Valley incision by debris flows: evidence of a topographic signature. Water Resour. Res. 39:103–132. http://dx.doi.org/10.1029/2001WR001057.
- St-Onge, G., Hillaire-Marcel, C., 2001. Isotopic constraints of sedimentary inputs and organic carbon burial rates in the Saguenay Fjord, Quebec. Mar. Geol. 176:1–22. http://dx.doi.org/10.1016/S0025-3227(01)00150-5.
- Van den Eeckhaut, M., Poesen, J., Govers, G., Verstraeten, G., Demoulin, A., 2007. Characteristics of the size distribution of recent and historical landslides in a populated hilly region. Earth Planet. Sci. Lett. 256:588–603. http://dx.doi.org/10.1016/j.epsl. 2007.01.040.
- Wang, K., Fialko, Y., 2015. Slip model of the 2015 M-w 7.8 Gorkha (Nepal) earthquake from inversions of ALOS-2 and GPS data. Geophys. Res. Lett. 42, 7452–7458.
- Wang, C.Y., Manga, M., 2015. New streams and springs after the 2014 Mw6. 0 South Napa earthquake. Nat. Commun. 6:7597. http://dx.doi.org/10.1038/ncomms8597.
- Wang, J., Jin, Z., Hilton, R.G., Zhang, F., Densmore, A.L., Li, G., West, A.J., 2015. Controls on Fluvial Evacuation of Sediment From Earthquake-Triggered Landslides. Geology 43: 115–118. http://dx.doi.org/10.1130/G36157.1.
- Wang, J., Jin, Z., Hilton, R.G., Zhang, F., Li, G., Densmore, A.L., Gröcke, D.R., Xu, X., West, A.J., 2016. Earthquake-triggered increase in biospheric carbon export from a mountain belt. Geology 44:471–474. http://dx.doi.org/10.1130/G37533.1.
- Wesnousky, S.G., Kumar, S., Mohindra, R., Thakur, V.C., 1999. Uplift and convergence along the Himalayan Frontal Thrust of India. Tectonics 18:967–976. http://dx.doi.org/10.1029/1999TC900026.

- West, A.J., Bickle, M.J., Collins, R., Brasington, J., 2002. Small-catchment perspective on Himalayan weathering fluxes. Geology 30, 355–358.

 Wobus, C.W., Hodges, K.V., Whipple, K.X., 2003. Has focused denudation sustained active thrusting at the Himalayan topographic front? Geology 31 (10):861–864. http://dx.
- thrusting at the Himalayan topographic front? Geology 51 (10),601–604. http://dx.doi.org/10.1130/G19730.1.

 Xu, C., Xu, X., Tian, Y., Shen, L., Yao, Q., Huang, X., Ma, J., Chen, X., Ma, S., 2016. Two comparable earthquakes produced greatly different coseismic landslides: The 2015 Gorkha, Nepal and 2008 Wenchuan, China events. J. Earth Sci. 27 (6):1008–1015. http://dx.doi.org/10.1007/s12583-016-0684-6.
- Zhang, S., Zhang, L.M., Xiang, B., Yuan, Q., 2013. In: Meehan, C., Pradel, D., Pando, M.A., Labuz, J.F. (Eds.), Travel Distances of Earthquake-induced Landslides. In Geo-Congress 2013: Stability and Performance of Slopes and Embankments III. Geotechnical Special Publication (GSP) 231, pp. 991 - 1001, American Society of Civil Engineers, Reston, VA. http://dx.doi.org/10.1061/9780784412787.101#sthash.hAVsV5Bv.dpuf.
- Zhao, B., 2015. April 2015 Nepal earthquake: observations and reflections. Nat. Hazards 80:1405–1410. http://dx.doi.org/10.1007/s11069-015-2001-6.